



## Possibly seismically triggered avalanches after the S1222a Marsquake and S1000a impact event

A. Lucas, I.J. Daubar, M. Le Teuff, Clement Perrin, T. Kawamura, L. Posiolova, P. Lognonné, S. Rodriguez, D. Giardini, G. Sainton, et al.

### ► To cite this version:

A. Lucas, I.J. Daubar, M. Le Teuff, Clement Perrin, T. Kawamura, et al.. Possibly seismically triggered avalanches after the S1222a Marsquake and S1000a impact event. *Icarus*, 2024, 411, pp.115942. 10.1016/j.icarus.2023.115942 . hal-04386179

**HAL Id: hal-04386179**

**<https://hal.science/hal-04386179>**

Submitted on 10 Jan 2024

**HAL** is a multi-disciplinary open access archive for the deposit and dissemination of scientific research documents, whether they are published or not. The documents may come from teaching and research institutions in France or abroad, or from public or private research centers.

L'archive ouverte pluridisciplinaire **HAL**, est destinée au dépôt et à la diffusion de documents scientifiques de niveau recherche, publiés ou non, émanant des établissements d'enseignement et de recherche français ou étrangers, des laboratoires publics ou privés.

# Possibly seismically triggered avalanches after the S1222a Marsquake and S1000a impact event

Lucas A.<sup>1</sup>, Daubar I. J.<sup>2</sup>, Le Teuff M.<sup>1</sup>, Perrin C.<sup>3</sup>, Kawamura T.<sup>1</sup>, Posiolova L.<sup>4</sup>, Lognonné  
P.<sup>1</sup>, Rodriguez S.<sup>1</sup>, Giardini D.<sup>5</sup>, Sainton G.<sup>1</sup>, Mangeney A.<sup>1</sup>, McEwen A.<sup>6</sup>

<sup>1</sup>Université Paris Cité, Institut de physique du globe de Paris, CNRS, F-75005, Paris, France

<sup>2</sup>Brown University, Providence, RI, USA

<sup>3</sup>Nantes Université, Université d'Angers, Le Mans Université, CNRS, UMR 6112, Laboratoire de Planétologie et

Géosciences, UAR 3281, Observatoire des Sciences de l'Univers de Nantes Atlantique, Nantes, France

<sup>4</sup>Malin Space Science System, San Diego, CA, USA

<sup>5</sup>ETH, Zurich, Switzerland

<sup>6</sup>U. Arizona, USA

## Key Points:

- On May 4, 2022, a major martian seismic event was recorded
- We identified possibly seismically induced dust avalanches in the area of the estimated epicenter
- We discuss avalanche triggering conditions and derive a possible epicenter location based on avalanche spatial density

---

Corresponding author: A. Lucas, [lucas@ipgp.fr](mailto:lucas@ipgp.fr)



## Abstract

Ground motion from seismic events detected by the SEIS/InSight seismometer on Mars could potentially trigger dust avalanches. Our research strongly suggests that the seismic event S1000a may have triggered a significant number of dust avalanches. In contrast, following the seismic event S1222a, there was only a modest increase in avalanche occurrences. Orbital observations of the area surrounding the projected location of the S1222a quake reveal notable topographic features, such as North-South ridges and impact craters. We utilize orbital imagery to evaluate the rate of avalanches and explore how the S1222a event might have influenced this rate. The S1222a event appears to be a plausible factor contributing to the observed increase in avalanches. Our further analysis of the epicenter location aims to clarify how it aligns with the avalanches' spatial distribution, offering insights into the regional topography.

## Plain Language Summary

We explore the potential effects of seismic aftermath on Mars, focusing on how large seismic events might trigger dust avalanches and mass wasting. Our analysis of orbital data reveals that the affected area is characterized by steep slopes, predominantly around crater walls, where dust accumulation is substantial. This geological setup makes the region particularly prone to dust avalanches. Large seismic events are known to cause ground acceleration, which can reduce material cohesion and friction, or increase tangential strain. These changes are conducive to mass wasting. Based on our research, we propose that the S1222a marsquake could be a primary factor contributing to the observed increase in avalanche activity, as evidenced by our analysis of orbital imagery. This finding sheds light on the dynamic interplay between seismic activity and surface processes on Mars.

## 1 Introduction

On May 4, 2022, a major seismic event named S1222a (Kawamura et al., 2023) was recorded by the SEIS instrument (Lognonné et al., 2019) of the InSight mission (Banerdt et al., 2020). It was an unprecedented marsquake in the SEIS recording period with an estimated moment magnitude of  $M_W^{Ma}$  4.7 (InSight Marsquake Service, 2022). In comparison, 95% of events recorded by SEIS since landing in November 2018 had a magnitude below 3.5 (Clinton et al., 2021; Böse et al., 2021; Ceylan et al., 2022; Knapmeyer et al., 2023). As for some of the InSight events, a location was estimated with a back-Azimuth (bearing from the event toward InSight) of  $101^\circ$  ( $96^\circ$ - $112^\circ$ ) and an epicentral distance  $\Delta = 37^\circ$  ( $\pm 1.6^\circ$ ) which places the event epicenter at the location of  $3.0^\circ\text{S}, 171.9^\circ\text{E}$  (Kawamura et al., 2023) (green star on Fig. 1). Other nearby locations for the epicenter have also been proposed (Panning et al., 2023; Kim et al., 2022) (Fig. 1). No new impact crater has been reported that could be the source of this event (Fernando et al., 2023). The region shows many topographic features including a few tectonic structures expressed as north-south wrinkle ridges (Knapmeyer et al., 2006) and impact craters (Fig. 1). To the east of this region, the only major structures are Appollinaris Patera, a Noachian volcano (Tanaka et al., 2014) about 200 km in diameter, and a large alluvial fan spanning southwards from the volcano's rim.

From orbital images, we identified dust avalanches (also known as slope streaks) in this region (orange symbols on Fig. 1). These are known active mass wasting processes occurring on Mars in several contexts (Ferguson & Lucchitta, 1984; Sullivan et al., 2001; Aharonson et al., 2003; Schorghofer et al., 2002, 2007; Schorghofer & King, 2011; Gerstell et al., 2004; Baratoux et al., 2006; Chuang et al., 2007; Bergonio et al., 2013; Heyer et al., 2019, 2020; Valantinas et al., 2021). They appear as relatively dark or bright streaks on steep dust-covered slopes and occur in regions with a high albedo and low to very low thermal inertia (Sullivan et al., 2001; Aharonson et al., 2003). Dust avalanches on Mars typically appear darker than the surrounding terrain. This is likely due to the removal of lighter-colored surface dust by the avalanches. When a slope streak is formed, loose dust and sand on the

surface are mobilized and cascade down the slope, exposing the darker, underlying material (Malin et al., 2007; Dundas, 2020). This material may be darker due to several factors, such as the presence of iron-rich minerals or alteration by weathering processes (Christensen et al., 2001). In addition, the removal of surface dust by the avalanches may expose a rougher, more textured surface, which can scatter and absorb more light, making the streak appear even darker. Many studies discuss possible triggering conditions and emplacement mechanisms. Purely dry avalanches of fine dust have been explored from the perspective of both observations (Schorghofer et al., 2007; Phillips et al., 2007; Dundas, 2020), and numerical simulations (Lucas, 2010). Spring discharge involving salty groundwater and/or brines in the shallow subsurface has been proposed (Ferris et al., 2002; Miyamoto, 2004; Head et al., 2007; Kreslavsky & Head, 2009; Bhardwaj et al., 2017, 2019). Other possible triggers include wind (Baratoux et al., 2006; Heyer et al., 2019), seismic activity from impacts or internal forces, or boulder track (Chuang et al., 2007) have been proposed.

While previous studies looked at boulder falls and associated tracks triggered by possible paleo-seismic activity (Roberts et al., 2012; Brown & Roberts, 2019), no previous work could have directly tested the possibility of seismically induced mass wasting on Mars due to a lack of seismic event records before the InSight mission. In the framework of the recent seismic events S1000a and S1222a, we investigate the effects of the induced ground acceleration aftermaths as a potential triggering mechanism for dust avalanches in the vicinity of the located epicenter. To do so, we conduct regional mapping of the avalanches from pre-event and post-event imagery in order to estimate the effect of the marsquake and impact crater on the rate of avalanches. We take into account possible biases due to the limited number of images, the time span between images, the sub-surface properties through thermal behavior, and the various sensitivities of each camera sensor.

## 2 Methods

### 2.1 Orbital data and mapping

As soon as the S1222a event was detected by SEIS and an estimate of the epicenter location was provided, we investigated orbital observations provided by the Context (CTX) and High Resolution Imaging Science Experiment (HiRISE) cameras (Malin et al., 2007; McEwen et al., 2007), both on board the Mars Reconnaissance Orbiter (MRO). Along with MRO imagery, we examine images from the Mars Global Surveyor (MGS)/Mars Orbiter Camera (MOC) (Malin et al., 1992), and THEMIS-Vis/Odyssey (Fergason et al., 2006). This led to a set of hundreds of images acquired before the seismic event. In addition, we requested new MRO observation over areas where we mapped avalanches inside the uncertainty area (Kawamura et al., 2023) (Fig. 1, Supp. Info text S1). At the time of writing this paper, a dozen HiRISE images and thirty new CTX observations were obtained, all acquired after the S1222a seismic event. In addition to imagery, we used Digital Terrain Models (DTMs) from both Mars Orbiter Laser Altimeter (MOLA, Smith et al. (2001)) and High Resolution Stereo Camera (HRSC, Neukum and Jaumann (2004)), the geological map from Tanaka et al. (2014) and the thermal inertia map (Christensen et al., 2004) (See Supp. Info. Text S2), which all provide contextual information. Note that Figure 1 specifically depicts the area covered by post-S1222a event CTX imagery. All the data have been combined into a Geographical Information System (GIS) in order to manually map all avalanches in the region of interest (Fig. 1), by two independent people (see Supp. Info. Text S1 for details on the imagery processing and mapping). The older observations, provided by both MOC and THEMIS-Vis, were only used for confirming the very low fading rate (Sullivan et al., 2001), being in good agreement with the dust activity reported in this region (Battalio & Wang, 2021).

### 2.2 Estimates of avalanche rate and statistics

Avalanche rate  $q$  is obtained from equation provided in Aharonson et al. (2003):

$$q = 100 \times \frac{\Delta n}{n \Delta t}, \quad (1)$$

where  $n$  is the total number of avalanches observed in both the two overlapping images,  $\Delta n$  being the newly observed avalanches on the recent image and not in the older image, and  $\Delta t$  being the time span between the two observations in Martian years. This rate  $q$  is expressed in % of new events/Martian year (Aharonson et al., 2003). This method has also been used by recent work (Heyer et al., 2019). The time periods between overlapping images in our database range from  $\sim 0.3$  to almost 7 martian years.

Finally we agglomerate avalanches in the same location (i.e. crater) and hence to compute the avalanche rate in each area where new events can be observed between two overlapping images. As opposed to a squared binning, hexagons are more similar to circles, hence they better translate data aggregation around the bin center. As most areas covered by avalanches in this region are impact craters, this provides a more valuable way to decipher the avalanche coverage.

### 3 Results and discussion

#### 3.1 Avalanches triggered after S1000a impact event

Before discussing S1222a event, we investigated S1000a impact event which occurred on September 18 2021, and left a crater over 150 m in diameter at  $38.1^\circ\text{N}; -79.87^\circ\text{E}$  (Fig. 2). This event was recorded by SEIS and then orbital imagery revealed its actual location. Its magnitude was estimated to be around  $M_w^{Ma} 4.1$ , hence about 25 times smaller than S1222a in energy (Ceylan et al., 2022; Posiolova et al., 2022). It should be noted that the location estimate from the seismic signal analysis was felt at approximately 130 km away from the actual location, as discussed in (Posiolova et al., 2022). By analysing all pre-event images including CTX, and HRSC and post-event HiRISE images, we could map a very large number of avalanches not seen in pre-event imagery. By looking back in time using all available images, including MOC/MGS, we observed that these areas were not covered by dust avalanches prior to the impact event (Fig. 2.).

We looked at the density distribution of the new avalanches (as seen on the post-event images and having the same brightness, hence the same age) as a function of their respective distance to the impact crater (histogram inset in Fig. 2). This distribution follows a bell-shaped curve. As seen on Earth, seismically triggered mass-wasting is absent very close to the epicenter, and increases at farther distances until it decreases again at the farthest distances (e.g., Tatard, 2010; Livio & Ferrario, 2020). Nonetheless, the mechanism here is different. It is very likely that the avalanches are triggered by secondary impacts, and not seismic waves. As an example of a typical scenario, ejecta leaving the primary impact at a velocity  $v = 200 \text{ m.s}^{-1}$ , with a launch angle of  $\theta = 45^\circ$ , will have a ballistic flight time  $t_f$  of 76 sec (i.e.,  $t_f = 2 \times v \sin \theta / g$ ), and will land at a distance  $d_l = 10.78 \text{ km}$  (neglecting the air friction,  $d_l = v \cos \theta \times t_f$ ). Hence, the histogram in the inset of figure 2 is similar to the statistical distribution of secondary ejecta impacting the ground. This correlation indicates those secondary impacts are a likely source for the avalanches. Of course, the S1000a event is an ideal case. First of all, we know the position of the epicenter perfectly well, thanks to the orbital imagery revealing the source crater. What's more, the presence of northeast-southwest trending ripples implies the presence of uniformly distributed topographic slopes as moving away from the impact crater, hence the avalanche susceptibility. Note that Burleigh et al. (2012) demonstrated that impact blast can trigger slope streaks. The S1000a event also shows that an impact with a seismic magnitude  $M_w^{Ma} 4.1$  can trigger a very large number of avalanches on Mars. As such, this is likely to be discussed more thoroughly in a following work which would evaluate the ballistic recomposition in order to evaluate potential effects of secondary impacts on the dust avalanche triggering. However, the ground accelerations caused

by a surface impact and a deep earthquake are not the same. So, in view of our results for the S1000a event, we discuss our results for S1222a in the following sections.

### 3.2 Avalanche rate increase in post-marsquake S1222a images

We analyzed all image pairs over the whole area of interest near the S1222a estimated epicenter. We identified 4532 avalanches (orange symbols in Figure 1). More than 200 avalanches were identified on pre-event images (over the 2005–2021 period), and 122 were identified on the post-event CTX images with respect to their 2005–2021 period counterparts respectively. An example is given in Figure 3-a. Note that, while doubtful avalanches may have been detected (e.g., yellow symbols in Fig. 3-a), we only took into account the robust observations of new avalanches (e.g., red symbols in Fig. 3-a). For the statistical robustness, we then derived avalanche rates  $q$  for each CTX/CTX pair only. When times series were available, we derived avalanche rate chronicles (Fig. 3-b). As exemplified on Fig. 3-b, a strong increase of  $q$  is observed after the S1222a event. Indeed, over the whole area of interest (Fig. 1), the pre-event rates (circles in fig. 3-c) lie around  $2.6\%.\text{MYear}^{-1}$  with a maximum value of  $6\%.\text{MYear}^{-1}$ , accounting for uncertainties following Aharonson et al. (2003). These values are in agreement with in previous estimated by Aharonson et al. (2003), and avalanche rates do not differ substantially across the region covered by our study. In contrast, post-event values of  $q$  show a significantly different distribution both spatially and in amplitude (Figure 3-c,d). While most rates still fall below 10%, we observe that in 9 places, the rates are  $>10\%$ , as high as 40% (excluding outlier, Figure 3-d). If we keep only the sub-10% values, the average is the same as that before the seismic event ( $2.6\%.\text{MYear}^{-1}$ ), and there is also no dependence on the epicentral distance. Interestingly, the highest post-event  $q$  ( $>20\%$ ) are found at the smallest distances from the epicenter of the S1222a event proposed by Kawamura et al. (2023). When relating the derived avalanche rate  $q$  to the epicentral distance  $\Delta$  with respect to the estimated location from Kawamura et al. (2023), we obtained a slight decreasing trend of  $q$  with  $\Delta$ . Finally we also verified that temporal sampling of the orbital images ( $\Delta t$ ) does not bias the avalanche rate estimates (Fig. 3-e).

To address the limited number of observations, we employed a permutation test, also known as bootstrapping (Efron & Tibshirani, 1993; Davison & Hinkley, 1997). This non-parametric approach does not rely on specific distribution assumptions about the data. We began by calculating the avalanche rate for each CTX/CTX pair for both pre-event and post-event observations, determining the mean difference as our observed statistic. Then, we merged the pre-event and post-event rates, treating them as a combined dataset without distinction of their original times. This pooled data was randomly shuffled to create new groups, preserving the original group sizes. We calculated the permuted test statistic by assessing the avalanche rate in this permuted data. This permutation process was iterated a million times, generating a distribution of test statistics under the hypothesis of no marsquake influence. Comparing our observed statistic to the 95% confidence interval derived from bootstrapping, we found that the post-event avalanche rates in all CTX observations exceeded 95% of the bootstrap statistic distribution. This indicates a significant increase in avalanche activity following the seismic event. However, it is important to note that the area studied includes locations possibly too distant from the epicenter to be affected by the marsquake. Focusing on rates exceeding  $6\%.\text{MYear}^{-1}$ , the post-marsquake rates surpassed the 99.98% confidence level. These findings, along with the detailed bootstrapping procedure, are outlined in Algorithm 1 and illustrated in Figure 4.

### 3.3 Effect of the relative thermal inertia

Subsurface properties at shallow depths can be analyzed through thermal inertia, which indicates how solar energy absorption and subsequent subsurface heat propagation relate to material properties. Thermal inertia is represented as  $\Gamma \equiv \sqrt{\kappa_e(1-p)\rho C(T)}$ , where  $\kappa_e$  denotes effective thermal conductivity,  $p$  is porosity,  $\rho$  represents density, and  $C(T)$  is the specific heat capacity. Therefore, low thermal inertia can indicate high porosity, low den-

**Algorithm 1:** Assessing Influence of marsquake on avalanche rate**Input:** Pre-event image pairs  $(n, \Delta n, \Delta t)$ **Input:** Post-event image pairs  $(n, \Delta n, \Delta t)$ Define the observed test statistic:  $\Delta n_{obs}$  (change in the number of avalanches),  $n_{obs}$  (number of avalanches), and  $\Delta t_{obs}$  (time difference between images);

Combine the before and after data into a single pool, disregarding their original labels;

Perform resampling with replacement: Randomly sample, with replacement, from the pooled data to create a bootstrap sample of the same size as the original data set. Repeat this process to generate a large number of bootstrap samples.

Calculate the test statistic for each bootstrap sample: Compute the rate of avalanches for each bootstrap sample, given by  $\frac{\Delta n_{boot}}{n_{boot} \Delta t_{boot}}$ ;

Calculate the bootstrap statistic distribution: Collect the calculated test statistics from step 4 to form the bootstrap distribution of the test statistic;

Calculate the confidence interval: Determine the desired confidence level (e.g., 95%).

Compute the lower and upper percentiles of the bootstrap distribution corresponding to the chosen confidence level;

**Output:** Assessment of marsquake influence

sity, small grain size, or a combination of these factors. As Sullivan et al. (2001); Aharonson et al. (2003) previously demonstrated, dust avalanches on Mars typically occur on steep slopes and are found in areas with low absolute thermal inertia. It's important to note that thermal inertia values are derived from models and assumptions, as detailed by Christensen et al. (2004). Due to significant variations between orbits, we calculate the ratio of the apparent value of thermal inertia at avalanche scar location with respect to the median value on the surrounding plains, and named hereafter  $\Gamma^* = \Gamma_{avalanche} / \Gamma_{plain}$  (see Supp. Info. Text S2). By examining  $\Gamma^*$ , we found that areas with the lowest values experience the most significant increases in avalanche rates (see Fig. 3-c). Specifically, when  $\Gamma^* \gg 1.5$ , post-event avalanche rates do not exceed pre-event rates. Conversely, an increase in  $q$  is observed when  $\Gamma^* < 1.5$ . This leads us to conclude that post-event avalanche susceptibility on Mars is primarily influenced by scarp locations with steep slopes and the lowest apparent thermal inertia. Such conditions correspond to the most unconsolidated terrains or areas with fine granular material.

**3.4 Epicentral distance and possible sources of the quake**

Although the epicentral distance is far from being the only parameter that controls the avalanche rates, it remains an important control factor (Tatard, 2010; Livio & Ferrario, 2020) (Supp. Info. Text S3 and S5). The reason is that the transition between a static state and a flowing state is modelled by introducing a threshold allowing the material to flow. This has been shown to quantitatively capture debris and rock avalanche morphodynamics on Mars (Lucas, 2010; Lucas & Mangeney, 2007; Lucas et al., 2011, 2014) (see Supp. Info. Text S3). Nonetheless, local geology, fractures, aftershocks and historical events will have a significant effect on the aftermaths of an earthquake by leading the slopes close to failure (Tatard, 2010; Livio & Ferrario, 2020; Chen et al., 2020; Rosser et al., 2021; Lombardo & Tanyas, 2022). Taking into account all these considerations, the rate would not be expected to be controlled only by epicentral distance. However, our constraints on the characteristics of the marsquake are weak, especially in terms of depth, focal mechanisms, and therefore the resulting ground acceleration. Our knowledge on the geological heterogeneity is also poorly constrained. Also, compared to terrestrial standards, this marsquake remains a small event. Nonetheless, small seismic events have shown to significantly increase the rate of landslides



on Earth (Martino et al., 2022). Indeed, recent studies show that even very small amplitude seismicity may trigger instabilities on metastable slopes (Bontemps et al., 2020; Durand et al., Minor revision).

Nonetheless, under the hypothesis that event S1222a did trigger avalanches, we considered the empirical model proposed by Livio and Ferrario (2020) which relates the distribution of triggered avalanches  $N_{ava}$  with the epicentral distance  $\Delta$ :

$$G(\mathbf{m}) = N_{ava} = a \exp \left[ - \left( \frac{\Delta - b}{c} \right)^2 \right], \quad (2)$$

where  $a$  is the amplitude of the distribution,  $b$  the distance of the peak amplitude and  $c$  the width of the distribution. While we do not have images just before and just after the event, we derived an estimation of the number of triggered avalanches from this relationship:

$$N_{ava} = \Delta n - \bar{q} \times n \Delta t / 100, \quad (3)$$

where  $\bar{q}$  is the long-term avalanche rate (i.e., we conservatively considered  $6\% \text{ MYear}^{-1}$ ). Because the avalanche susceptibility is not evenly distributed (i.e., steep slopes only located inside impact craters, non-homogeneous surface/sub-surface properties), we only consider observations that meet the following criteria:  $\Gamma^* < 1.93$ , and  $\Delta t < 1.5 \text{ MYear}$ , to only account for the lowest thermal inertia (see Fig. 3) and the smallest time span between images to reduce biases. Then, we used a Monte Carlo method to invert the most probable epicenter location using a maximum likelihood function with a Laplacian distribution of errors (Mosegaard & Tarantola, 1995) (See Supp. Info. Text S4). The resulting probability distribution of the epicenter under all of these considerations is given in Figure 5. It is situated in between the locations obtained from both body and surface waves analysis respectively (Kawamura et al., 2023; Panning et al., 2023; Kim et al., 2022), then included in the uncertainty ellipses of epicentral locations (green contours in Fig. 5).

This distribution can lead us to two different interpretations regarding the source mechanism of the quake, mainly related to internal tectonic activity. A first hypothesis would be based on the fact that our distribution is slightly shifted toward the East from the wrinkle ridges, on the flanks of Apollinaris Patera. It is now well supported that Mars still hosts remnant volcano-tectonic activity, especially along Cerberus Fossae (Giardini et al., 2020; Horvath et al., 2021; Perrin et al., 2022; Stähler et al., 2022), possibly due to the presence of a plume (Broquet & Andrews-Hanna, 2022), and associated with normal slip motion (Brinkman et al., 2021; Jacob et al., 2022). While the moment tensor analysis of the S1222a event can give very different slip motions, NNW-SSE normal faulting is a possible solution (Maguire et al., 2023), highlighting a possible activity of Apollinaris Patera at depth. However, unlike Cerberus Fossae, Apollinaris Patera is an old Noachian volcano, thus it seems unlikely that remnant volcanic activity would be present at shallow depth. A second hypothesis would be related to the 450 km long wrinkle ridge, trending NNE-SSW, and cross-cutting the Hesperian terrains between the two epicentral locations (black lines in figure 5). The probability distribution of the epicenter inferred from the avalanche rate is about 30 to 60 km East of this major structure. The shape of the topographic profile across the ridge is an asymmetric arch-ridge, with a steep slope facing West and a shallow slope facing East (Fig. 1), which would imply a main East-dipping thrust at depth (Andrews-Hanna, 2020). Assuming a fault dip of  $34^\circ$  to  $42^\circ$  for arch-ridges (Andrews-Hanna, 2020), a probability distribution situated about 30 to 60 km East of the wrinkle ridge would lead to a hypocentral depth ranging from 20 to 54 km. This range of depth is in agreement with the best solutions found by Maguire et al. (2023). Along with another study by (Brinkman et al., 2023), their preferred solutions present mainly reverse slip motions striking E-W to NW-SE, which is not optimally oriented with the overall wrinkle ridge observed from orbital imagery. However, local large variations in fault strikes are possible along a wrinkle ridge. Note that the wrinkle ridges are cross-cutting a large E-W bulge situated at about  $-5^\circ$  latitude, connecting the flanks of Apollinaris Patera and a large crater in the west (Fig. 1). This bulge presents hundreds of meters

of difference in elevation and slight apparent thermal inertia anomalies that could indicate a bedrock affected by an old tectonic structure. Interestingly, the bulge's azimuth is aligned with our probability distribution of the epicenter. More work would be needed to understand the origin of this structure and a possible link with the source of the marsquake.

It should also be noted that source locations obtained from other methods such as surface waves or coda characteristics give different locations (Kim et al., 2022; Panning et al., 2023; Menina et al., 2023). Both studies using surface waves predict source locations more towards the south as shown in 5. This is due to different back azimuth they obtained for surface waves compared from that described in (Kawamura et al., 2023) using body waves. Panning et al. (2023) also discusses the possibility that the source location could be in the southern hemisphere. Interestingly, Menina et al. (2023) conclude that they need a thick (60km) diffusive layer to explain the coda shape of S1222a. This could imply that either the source location could be in the highlands of the southern hemisphere (Wieczorek et al., 2022), or that thermal anomalies at depth are present in the Appollinaris area.

Our work leads us to propose that the source of the quake is likely due to thermal contraction due to Mars' cooling through time. The peak of thermal contraction and wrinkle ridge formation occurred during the early Hesperian and decreased progressively until now (Watters, 1993). Even if the wrinkle ridge in figure 5 is well expressed in morphology, its surface trace ends to the north, near the transition between Hesperian and Amazonian terrains (Tanaka et al., 2014). This indicates that the ridge has not been active in recent times. However, thermal contraction is still ongoing on Mars and might re-activate local mechanical weaknesses in the martian crust, such as wrinkle ridges, over larger recurrence time periods. If such activity is real, microseismicity should be associated with it.

## 4 Conclusions

In our comprehensive study of surface features surrounding the S1000a and S1222a seismic events on Mars, we utilized MRO orbital data to assess the associated avalanche rates. Our findings reveal a substantial increase in avalanches following the S1000a impact event, suggesting its indirect aftermaths, likely via secondary impacts. The S1222a event presented a more complex scenario, necessitating thorough investigation. We established pre-event avalanche rates in line with global estimates from Aharonson et al. (2003) and those near Olympus Mons obtained by Heyer et al. (2019), ranging between 1 and 6%.MYears<sup>-1</sup>. These rates, when compared to post-event rates of up to 40%.MYear<sup>-1</sup> near the estimated epicenter (Kawamura et al., 2023; Panning et al., 2023; Kim et al., 2022), underscore a significant increase in areas of lower apparent thermal inertia. This leads us to propose that the S1222a marsquake could be the driving factor behind the observed increase in avalanches. This analysis also enabled us to estimate a probable epicenter for the marsquake, considering the  $\Gamma^*$  threshold of 1.5 and a radial ground acceleration. This inferred location is intriguingly situated near a volcanic edifice and a North-South wrinkle ridge, highlighting the geological complexity of the region. Our study not only might suggest that current seismic activity on Mars can initiate mass wasting processes like dust avalanches but also opens avenues for exploring regions with observed avalanches and other seismic events detected by the InSight mission. The increased rates of avalanches in areas with historical seismic sources suggest that ground deformation plays a pivotal role in these phenomena. This methodology can be invaluable in future seismic event analyses, where visible aftermaths such as avalanches can offer significant insights into epicenter locations. Overall, our findings demonstrate that avalanches on Mars serve as a crucial tool for documenting rapid processes, from discrete surface perturbations like impacts to more continuous events like quakes. This understanding significantly enhances our ability to study and interpret the dynamic surface and subsurface processes of Mars.

## 5 Acknowledgments

Authors thank Menina S., Margerin L., Kim D., Malystskyy D., Stähler S., Wieczorek M., Panning M. for InSightful discussions on the S1222a event. Authors thank Dundas C.M. for his help in accessing the post-event HiRISE images for both events. The authors express their gratitude to Ferrari C. for providing valuable insights into thermal inertia, to A. Spiga for his expertise on the output of General Circulation Models (GCMs), and to P. Souloumiac for her expert knowledge on slope failure conditions. Authors thank anonymous reviewers and the associate editor for their constructive feedback that substantially improved the manuscript. All authors declare no conflict of interest. French co-authors acknowledge the French Space Agency CNES and ANR (ANR-19-CE31-0008). AL, TK, PL, SR, GS, AM acknowledge Idex Paris Cité (ANR-18-IDEX-0001). IJD was funded by NASA InSight PSP grant 80NSSC20K0971.

## 6 Open Research

The orbital data are available online: HRSC are available at ESA's Planetary Science Archive (<https://www.cosmos.esa.int/web/psa/mars-express>). THEMIS data are available at Arizona State University's repository (<https://themis.asu.edu>). MOC images are available at the PDS Imaging Node ([https://pds-imaging.jpl.nasa.gov/data/mgs-m-moc-na\\_wa-2-sdp-l0-v1.0/](https://pds-imaging.jpl.nasa.gov/data/mgs-m-moc-na_wa-2-sdp-l0-v1.0/)). MOLA data are available at the PDS Geosciences Node (<https://pds-geosciences.wustl.edu/missions/mgs/mola.html>). Apparent thermal inertia map is provided by the USGS (<https://astrogeology.usgs.gov/maps/mars-themis-derived-global-thermal-inertia-mosaic>). HiRISE data, including the post-event images, are available at the University of Arizona's dedicated website (<https://www.uahirise.org>). CTX image are available at the Imaging PDS Node ([https://pds-imaging.jpl.nasa.gov/data/mro/mars\\_reconnaissance\\_orbiter/ctx/](https://pds-imaging.jpl.nasa.gov/data/mro/mars_reconnaissance_orbiter/ctx/)). The post-event CTX images will be posted on the NASA PDS by MSSS by the time of publication. Meanwhile, referee's can have access to the mosaic at <https://www.dropbox.com/sh/ulcykaotwxvi7ga/AAAsDcqw4FrkGDqjb4HTFmjka?dl=0>. The avalanche catalogue is available on Zenodo (doi:10.5281/zenodo.7679315). The InSight seismic event catalogue version 9 (InSight Marsquake Service, 2022) and waveform data (InSight Mars SEIS Data Service, 2019a,b) are available from the IGP Datacenter and IRIS-DMC, as are previous catalogue versions. Seismic waveforms are also available from NASA PDS. The crustal thickness grid is available on Zenodo (doi:10.5281/zenodo.6477509).



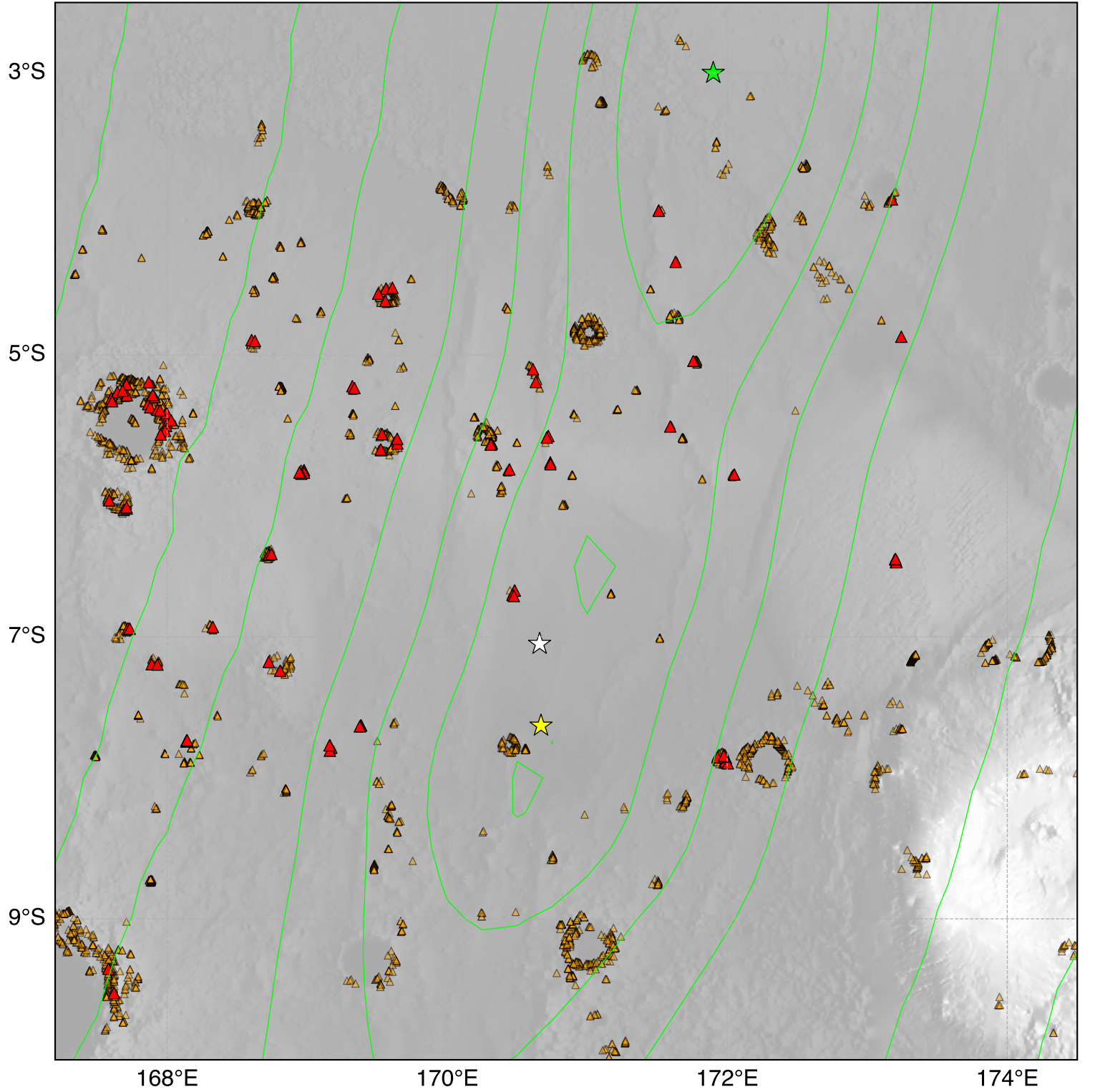


**Figure 1.** Regional map of dust avalanches near the S1222a event estimated location (green star with associated green contours, (Kawamura et al., 2023)). The white star is the location estimated by multi-orbit surface waves (Panning et al., 2023). The yellow star shows the estimated location according to surface waves (Kim et al., 2022). Orange symbols are all avalanches mapped. Red symbols show where avalanches are observed on post-event images. Basemap is the MOLA elevation map (Smith et al., 2001).

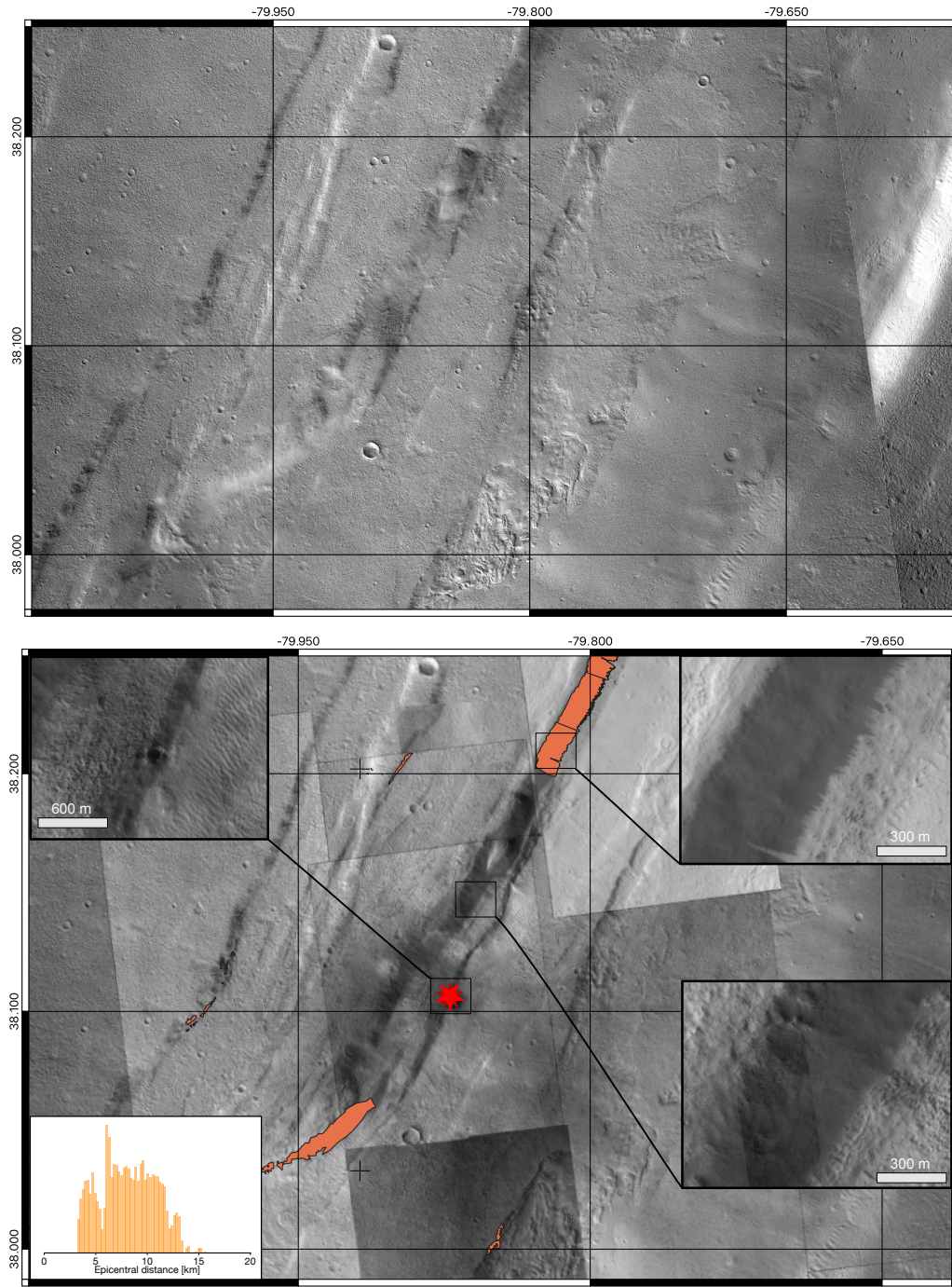


**Figure 2.** (top) Pre-event CTX mosaic around the impact location of S1000a (dated from 2018-09-12) showing absence of any dust avalanches. (bottom) Post-event HiRISE mosaic on top of CTX images around the impact location of S1000a event (red star) with associated triggered avalanches (orange areas). Insets show close-up on the crater, the avalanches areas and slopes without new avalanches (from top-left, to bottom-right, respectively). The density distribution of avalanches with respect to the epicentral distance is shown in the bottom-left inset.

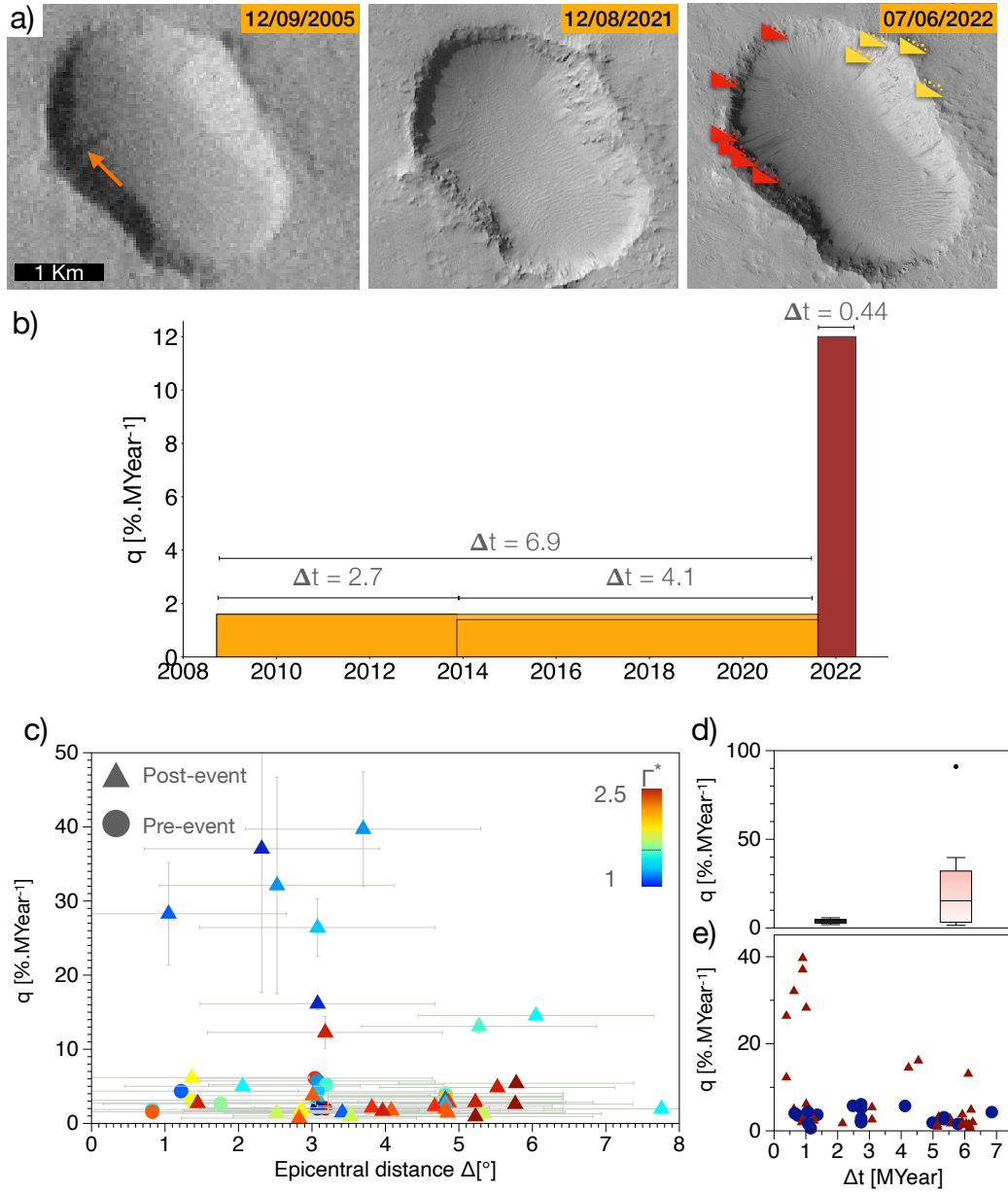


**Figure 3.** a) Image times series with THEMIS-Vis image V1768100 (17m/pixel) taken in 2005, CTX image N21\_070520\_1744\_XI\_05S189W (6m/pixel) taken 8 months before S1222a, and an HiRISE image (down-sampled to 5m/pixel) ESP\_074357\_1745 taken a few weeks after the marsquake. New avalanches marked with the red symbols. Additional doubtful avalanches are indicated with the yellow symbols, b) time series of avalanche rate  $q$  over the 2008-2022 period (orange for pre-event period, red for image pair including post-event observations). c) Avalanche rate  $q$  as a function of the epicentral distance  $\Delta$  (with respect to the green star of Fig. 1) for CTX/CTX image pairs. Symbols are associated to pre-event (circles) or post-event (triangles). Color scales with the ratio of apparent thermal inertia ( $\Gamma^*$ , with dashed line at 1.5). d) Box plot of avalanche rates for pre-event pairs (black) and pre/post-event pairs (red). e) Avalanche rate  $q$  as a function of timespan  $\Delta t$ . Note that some symbols can overlap each other on both plots.

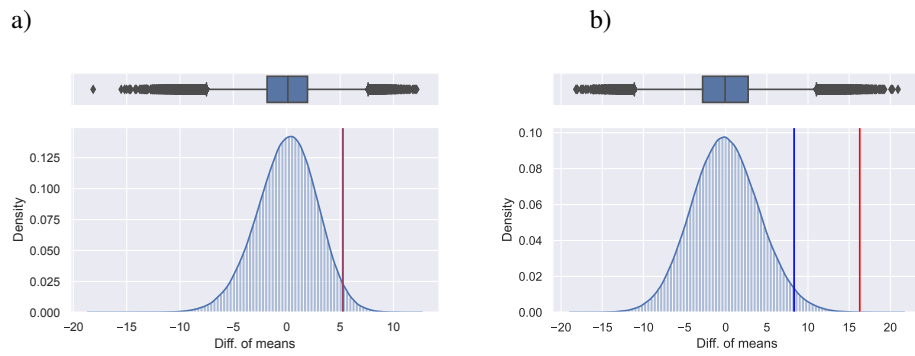


**Figure 4.** Bootstrapping statistics. (a) accounting for the whole data set, (b) when only considering  $q > 5$  for the post-event observation. (top-panel) Quantiles of the permutation tests. (bottom-panel) The distribution of the permutation tests. The thin vertical blue lines gives the 95% of the test statistics distribution. The dashed red vertical line shows the observed statistics.



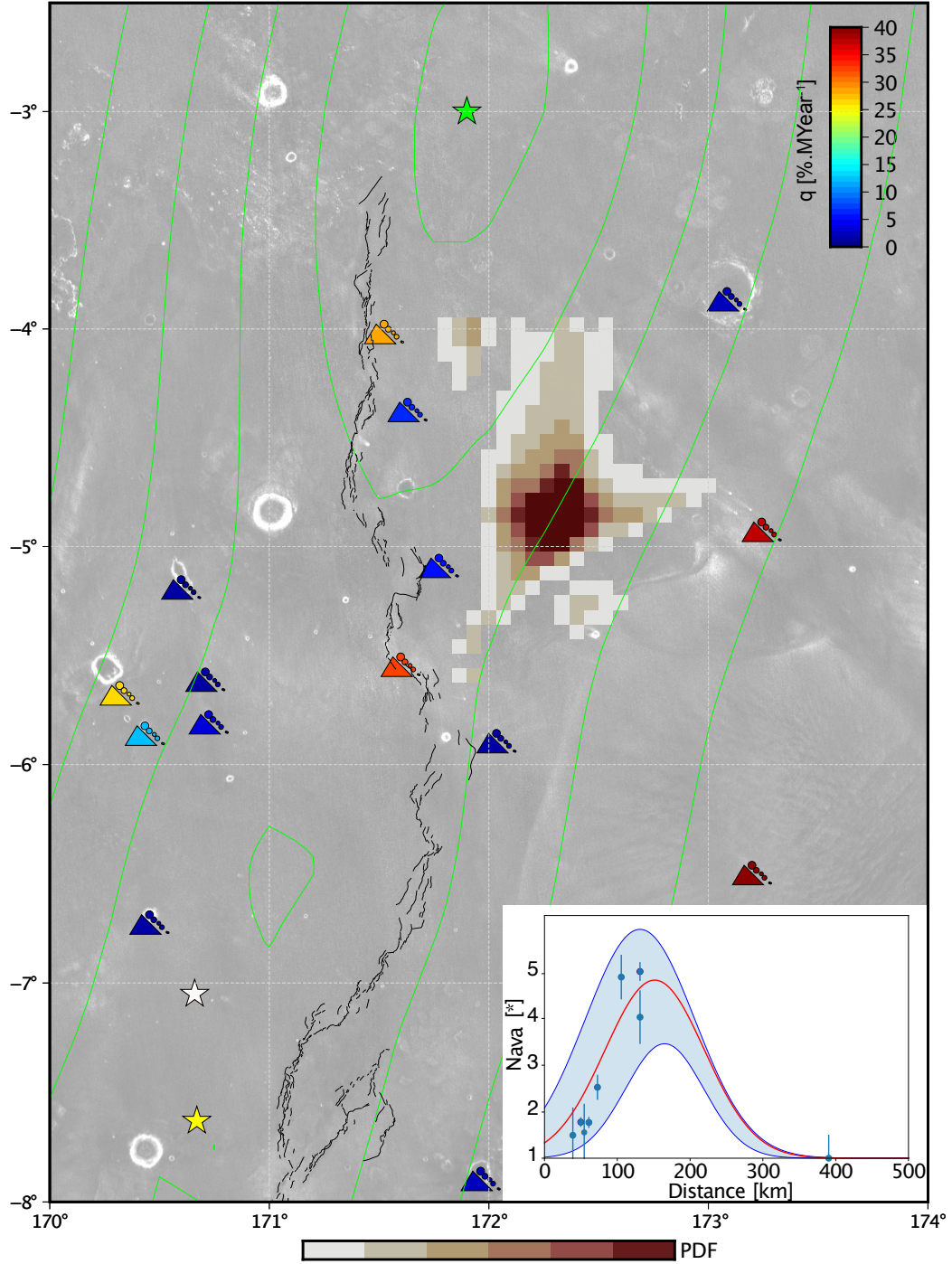


**Figure 5.** Probability distribution of the epicenter inferred from avalanche observations (reddish colormap). Symbols show number of avalanches observed on post-event images. Color scales with the rate  $q$ . The green star (upper center) is the maximum peak of the estimated epicenter and its uncertainty ellipses (green contours) obtained from body waves (Kawamura et al., 2023), the white star, the location estimated from multi-orbit surface waves (Panning et al., 2023), and the yellow star is the estimated epicenter derived from the surface waves (Kim et al., 2022). Black lines are detailed surface traces of the main wrinkle ridge in the vicinity of the epicentral area. Background map is the thermal inertia  $\Gamma$ . (Inset) Expected avalanche density distribution with confidence interval from Monte Carlo inversion using equation 2 with respect to the number of avalanche  $N_{ava}$  derived from equation 3.

## References

- Aharonson, O., Schorghofer, N., & Gerstell, M. F. (2003). Slope streak formation and dust deposition rates on Mars: Martian slope streak formation rates. *Journal of Geophysical Research: Planets*, 108(E12). Retrieved 2022-07-14, from <http://doi.wiley.com/10.1029/2003JE002123> doi: 10.1029/2003JE002123
- Andrews-Hanna, J. C. (2020). The tectonic architecture of wrinkle ridges on Mars. *Icarus*, 351(October 2019), 113937. Retrieved from <https://doi.org/10.1016/j.icarus.2020.113937> doi: 10.1016/j.icarus.2020.113937
- Banerdt, W. B., Smrekar, S. E., Banfield, D., Giardini, D., Golombek, M., Johnson, C. L., ... Wieczorek, M. (2020, Mar 01). Initial results from the insight mission on mars. *Nature Geoscience*, 13(3), 183-189.
- Baratoux, D., Mangold, N., Forget, F., Cord, A., Pinet, P., Daydou, Y., ... HRSC CO-Investigator Team (2006). The role of the wind-transported dust in slope streaks activity: Evidence from the HRSC data. *Icarus*, 183(1), 30-45. doi: 10.1016/j.icarus.2006.01.023
- Battalio, M., & Wang, H. (2021). The Mars Dust Activity Database (MDAD): A comprehensive statistical study of dust storm sequences. *Icarus*, 354, 114059. Retrieved 2022-07-14, from <https://linkinghub.elsevier.com/retrieve/pii/S001910352030405X> doi: 10.1016/j.icarus.2020.114059
- Bergonio, J. R., Rottas, K. M., & Schorghofer, N. (2013). Properties of martian slope streak populations. *Icarus*, 225(1), 194-199. Retrieved from <https://www.sciencedirect.com/science/article/pii/S0019103513001395> doi: <https://doi.org/10.1016/j.icarus.2013.03.023>
- Bhardwaj, A., Sam, L., Martín-Torres, F. J., Zorzano, M.-P., & Fonseca, R. M. (2017). Martian slope streaks as plausible indicators of transient water activity. *Scientific Reports*, 7(1), 7074. Retrieved from <https://doi.org/10.1038/s41598-017-07453-9> doi: 10.1038/s41598-017-07453-9
- Bhardwaj, A., Sam, L., Martín-Torres, F. J., & Zorzano, M.-P. (2019). Are slope streaks indicative of global-scale aqueous processes on contemporary mars? *Reviews of Geophysics*, 57(1), 48-77. doi: <https://doi.org/10.1029/2018RG000617>
- Bontemps, N., Lacroix, P., Larose, E., Jara, J., & Taïpe, E. (2020). Rain and small earthquakes maintain a slow-moving landslide in a persistent critical state. *Nature Communications*, 11(1), 780.
- Brinkman, N., Sollberger, D., Schmelzbach, C., Stähler, S. C., & Robertsson, J. (2023). Applications of time-frequency domain polarization filtering to insight seismic data. *Earth and Space Science*, 10(11), e2023EA003169.
- Brinkman, N., Stähler, S. C., Giardini, D., Schmelzbach, C., Khan, A., Jacob, A., ... Banerdt, W. B. (2021). First focal mechanisms of marsquakes. *Journal of Geophysical Research: Planets*. Retrieved from <https://agupubs.onlinelibrary.wiley.com/doi/abs/10.1029/2020JE006546> doi: <https://doi.org/10.1029/2020JE006546>
- Broquet, A., & Andrews-Hanna, J. C. (2022). Geophysical evidence for an active mantle plume underneath Elysium Planitia on Mars. *Nature Astronomy*. doi: 10.1038/s41550-022-01836-3
- Brown, J., & Roberts, G. (2019). Possible evidence for variation in magnitude for marsquakes from fallen boulder populations, Grjota Valles, Mars. *J. Geophys. Res. Planets*, 124(3), 801-812. doi: 10.1029/2018JE005622
- Burleigh, K. J., Melosh, H. J., Tornabene, L. L., Ivanov, B., McEwen, A. S., & Daubar, I. J. (2012). Impact airblast triggers dust avalanches on mars. *Icarus*, 217(1), 194-201.
- Böse, M., Stähler, S. C., Deichmann, N., Giardini, D., Clinton, J., Lognonné, P., ... Banerdt, W. B. (2021, 06). Magnitude Scales for Marsquakes Calibrated from InSight Data. *Bulletin of the Seismological Society of America*, 111(6), 3003-3015.
- Ceylan, S., Clinton, J. F., Giardini, D., Stähler, S. C., Horleston, A., Kawamura, T., ... Banerdt, W. B. (2022). The marsquake catalogue from insight, sols 0–1011. *Physics of the Earth and Planetary Interiors*, 333, 106943.

- Chen, X.-l., Shan, X., Wang, M.-m., Liu, C.-g., & Han, N.-n. (2020, 03). Distribution pattern of coseismic landslides triggered by the 2017 jiuzhaigou ms 7.0 earthquake of china: Control of seismic landslide susceptibility. *ISPRS International Journal of Geo-Information*, 9, 198. doi: 10.3390/ijgi9040198
- Christensen, P. R., Bandfield, J. L., Hamilton, V. E., Ruff, S. W., Kieffer, H. H., Titus, T. N., ... Greenfield, M. (2001). Mars global surveyor thermal emission spectrometer experiment: Investigation description and surface science results. *Journal of Geophysical Research: Planets*, 106(E10), 23823-23871.
- Christensen, P. R., Jakosky, B. M., Kieffer, H. H., Malin, M. C., Jr, H. Y. M., Nealon, K., ... Ravine, M. (2004). The thermal emission imaging system (themis) for the mars 2001 odyssey mission. In C. T. Russell (Ed.), *2001 mars odyssey* (pp. 85–130). Dordrecht: Springer Netherlands.
- Chuang, F. C., Beyer, R. A., McEwen, A. S., & Thomson, B. J. (2007). HiRISE observations of slope streaks on mars. *Geophysical Research Letters*, 34(20). Retrieved from <https://agupubs.onlinelibrary.wiley.com/doi/abs/10.1029/2007GL031111> doi: <https://doi.org/10.1029/2007GL031111>
- Clinton, J. F., Ceylan, S., van Driel, M., Giardini, D., Stähler, S. C., Böse, M., ... Stott, A. E. (2021). The marsquake catalogue from insight, sols 0–478. *Physics of the Earth and Planetary Interiors*, 310, 106595.
- Davison, A. C., & Hinkley, D. V. (1997). *Bootstrap methods and their application*. Cambridge University Press.
- Dundas, C. M. (2020). Geomorphological evidence for a dry dust avalanche origin of slope streaks on mars. *Nature Geoscience*, 13(7), 473–476. Retrieved from <https://doi.org/10.1038/s41561-020-0598-x> doi: 10.1038/s41561-020-0598-x
- Durand, V., Mangeney, A., Bernard, P., Bonilla, L. F., Satriano, C., Jia, X., ... Hibert, C. (Minor revision). The competing role of seismicity and rainfall in slope destabilization: rockfalls triggered on a metastable volcanic edifice. *Science Advances*.
- Efron, B., & Tibshirani, R. J. (1993). *An introduction to the bootstrap*. CRC Press.
- Ferguson, R. L., Christensen, P. R., & Kieffer, H. H. (2006, dec). High-resolution thermal inertia derived from the Thermal Emission Imaging System (THEMIS): Thermal model and applications. *Journal of Geophysical Research: Planets*, 111(E12), n/a–n/a. Retrieved from <http://doi.wiley.com/10.1029/2006JE002735> doi: 10.1029/2006JE002735
- Ferguson, H. M., & Lucchitta, B. K. (1984). *Dark streaks on talus slopes, Mars*. In NASA. Washington Rept. of Planetary Geol. Programs p 188-190 (SEE N84-23431 13-91).
- Fernando, B., Daubar, I. J., Charalambous, C., Grindrod, P. M., Stott, A., Al Ateqi, A., ... Banerdt, W. B. (2023). A Tectonic Origin for the Largest Marsquake Observed by InSight. *Geophysical Research Letters*, 50(20), 1–10. doi: 10.1029/2023GL103619
- Ferris, J. C., Dohm, J. M., Baker, V. R., & Maddock III, T. (2002). Dark slope streaks on mars: Are aqueous processes involved? *Geophysical Research Letters*, 29(10), 128-1-128-4. Retrieved from <https://agupubs.onlinelibrary.wiley.com/doi/abs/10.1029/2002GL014936> doi: <https://doi.org/10.1029/2002GL014936>
- Gerstell, M. F., Aharonson, O., & Schorghofer, N. (2004). A distinct class of avalanche scars on Mars. *Icarus*, 168(1), 122–130. Retrieved 2022-07-14, from <https://linkinghub.elsevier.com/retrieve/pii/S0019103503003907> doi: 10.1016/j.icarus.2003.11.005
- Giardini, D., Lognonné, P., Banerdt, W., Pike, W., Christensen, U., Ceylan, S., ... Yana., C. (2020). The Seismicity of Mars. *Nature Geoscience*, 13(3), 205–212. doi: <http://doi.org/10.1038/s41561-020-0539-8>
- Head, J. W., Marchant, D. R., Dickson, J. L., Levy, J. S., & Morgan, G. A. (2007, March). Slope Streaks in the Antarctic Dry Valleys: Characteristics, Candidate Formation Mechanisms, and Implications for Slope Streak Formation in the Martian Environment. In *38th annual lunar and planetary science conference* (p. 1935).
- Heyer, T., Kreslavsky, M., Hiesinger, H., Reiss, D., Bernhardt, H., & Jaumann, R. (2019).

- Seasonal formation rates of martian slope streaks. *Icarus*, 323, 76–86. Retrieved 2022-07-14, from <https://linkinghub.elsevier.com/retrieve/pii/S0019103518306857> doi: 10.1016/j.icarus.2019.01.010
- Heyer, T., Raack, J., Hiesinger, H., & Jaumann, R. (2020). Dust devil triggering of slope streaks on mars. *Icarus*, 351, 113951. Retrieved from <https://www.sciencedirect.com/science/article/pii/S0019103520303249> doi: <https://doi.org/10.1016/j.icarus.2020.113951>
- Horvath, D. G., Moitra, P., Hamilton, C. W., Craddock, R. A., & Andrews-Hanna, J. C. (2021, September). Evidence for geologically recent explosive volcanism in Elysium Planitia, Mars. *Icarus*, 365, 114499. doi: 10.1016/j.icarus.2021.114499
- InSight Marsquake Service. (2022). *Mars seismic catalogue, insight mission; v12 2022-10-01*. ETHZ, IGP, JPL, ICL, Univ. Bristol. Retrieved from <https://www.insight.ethz.ch/seismicity/catalog/v12> doi: 10.12686/a18
- Jacob, A., Plasman, M., Perrin, C., Fuji, N., Lognonné, P., Xu, Z., ... Banerdt, W. (2022). Seismic sources of insight marsquakes and seismotectonic context of elysium planitia, mars. *Tectonophysics*, 837, 229434. Retrieved from <https://www.sciencedirect.com/science/article/pii/S0040195122002281> doi: <https://doi.org/10.1016/j.tecto.2022.229434>
- Kawamura, T., Clinton, J., Zenhäusern, G., Ceylan, S., Horleston, A., Dahmen, N., ... Banerdt, W. (2023). S1222a - the largest Marsquake detected by InSight. *Geophysical Research Letters*. doi: 10.1029/2022GL101543
- Kim, D., Stähler, S. C., Ceylan, S., Lekic, V., Maguire, R., Zenhäusern, G., ... Banerdt, W. B. (2022). Structure along the martian dichotomy constrained by rayleigh and love waves and their overtones. *Geophysical Research Letters*, e2022GL101666.
- Knapmeyer, M., Oberst, J., Hauber, E., Wählisch, M., Deuchler, C., & Wagner, R. (2006). Working models for spatial distribution and level of Mars' seismicity. *J. Geophys. Res. E Planets*, 111(11), 1–23. doi: 10.1029/2006JE002708
- Knapmeyer, M., Stähler, S., Plesa, A.-C., Ceylan, S., Charalambous, C., Clinton, J., ... Banerdt, W. B. (2023). The global seismic moment rate of mars after event s1222a. *Geophysical Research Letters*, 50(7), e2022GL102296.
- Kreslavsky, M. A., & Head, J. W. (2009). Slope streaks on Mars: A new "wet" mechanism. *Icarus*, 201(2), 517–527. Retrieved 2022-07-14, from <https://linkinghub.elsevier.com/retrieve/pii/S0019103509000608> doi: 10.1016/j.icarus.2009.01.026
- Livio, F., & Ferrario, M. F. (2020). Assessment of attenuation regressions for earthquake-triggered landslides in the italian apennines: insights from recent and historical events. *Landslides*, 17(12), 2825–2836.
- Lognonné, P., Banerdt, W. B., Giardini, D., Pike, W. T., Christensen, U., Laudet, P., ... Wookey, J. (2019, feb). SEIS: Insight's Seismic Experiment for Internal Structure of Mars. *Space Science Reviews*, 215(1), 12. Retrieved from <http://dx.doi.org/10.1007/s11214-018-0574-6> <http://link.springer.com/10.1007/s11214-018-0574-6> doi: 10.1007/s11214-018-0574-6
- Lombardo, L., & Tanyas, H. (2022). From scenario-based seismic hazard to scenario-based landslide hazard: fast-forwarding to the future via statistical simulations. *Stoch Environ Res Risk Assess*, 36, 2229–2242.
- Lucas, A. (2010). *Dynamique des instabilités gravitaires par modélisation et télédétection: Applications aux exemples martiens* (Theses, Institut de physique du globe de paris - IGP). Retrieved from <https://tel.archives-ouvertes.fr/tel-00503212>
- Lucas, A., & Mangeney, A. (2007). Mobility and topographic effects for large valles marineris landslides on mars. *Geophysical Research Letters*, 34(10).
- Lucas, A., Mangeney, A., & Ampuero, J. P. (2014). Frictional velocity-weakening in landslides on earth and on other planetary bodies. *Nature Communications*, 5(1), 3417.
- Lucas, A., Mangeney, A., Mège, D., & Bouchut, F. (2011). Influence of the scar geometry on landslide dynamics and deposits: Application to martian landslides. *Journal of*



- Geophysical Research: Planets*, 116(E10).
- Maguire, R. R., Lekić, V., Schmerr, N. C., Kim, D., Li, J., Beghein, C., . . . Bruce Banerdt, W. (2023). Moment Tensor Estimation of Event S1222a and Implications for Tectonics Near the Dichotomy Boundary in Southern Elysium Planitia Mars. *Journal of Geophysical Research E: Planets*, submitted.
- Malin, M. C., Bell, J. F., Cantor, B. A., Caplinger, M. A., Calvin, W. M., Clancy, R. T., . . . Wolff, M. J. (2007, may). Context Camera Investigation on board the Mars Reconnaissance Orbiter. *Journal of Geophysical Research*, 112(E5), E05S04. Retrieved from <http://doi.wiley.com/10.1029/2006JE002808> doi: 10.1029/2006JE002808
- Malin, M. C., Danielson, G. E., Ingersoll, A. P., Masursky, H., Veverka, J., Ravine, M. A., & Soulanille, T. A. (1992). Mars observer camera. *Journal of Geophysical Research: Planets*, 97(E5), 7699-7718.
- Martino, S., Fiorucci, M., Marmoni, G. M., Casaburi, L., Antonielli, B., & Mazzanti, P. (2022). Increase in landslide activity after a low-magnitude earthquake as inferred from dInSAR interferometry. *Scientific Reports*, 12(1), 2686.
- McEwen, A. S., Eliason, E. M., Bergstrom, J. W., Bridges, N. T., Hansen, C. J., Delamere, W. A., . . . Weitz, C. M. (2007, may). Mars Reconnaissance Orbiter's High Resolution Imaging Science Experiment (HiRISE). *Journal of Geophysical Research*, 112(E5), E05S02. Retrieved from <http://doi.wiley.com/10.1029/2005JE002605> doi: 10.1029/2005JE002605
- Menina, S., Margerin, L., Kawamura, T., Heller, G., Drilleau, M., Xu, Z., . . . Banerdt, W. B. (2023). Stratification of heterogeneity in the lithosphere of Mars from envelope modeling of event S1222a and near impacts: Interpretation and implications for very-high-frequency events. *Geophysical Research Letters*, 50(7), e2023GL103202.
- Miyamoto, H. (2004). Fluid dynamical implications of anastomosing slope streaks on Mars. *Journal of Geophysical Research*, 109(E6), E06008. Retrieved 2022-07-14, from <http://doi.wiley.com/10.1029/2003JE002234> doi: 10.1029/2003JE002234
- Mosegaard, K., & Tarantola, A. (1995). Monte carlo sampling of solutions to inverse problems. *Journal of Geophysical Research: Solid Earth*, 100(B7), 12431-12447. doi: <https://doi.org/10.1029/94JB03097>
- Neukum, G., & Jaumann, R. (2004). The high resolution stereo camera of Mars Express. *ESA Special Publication*, 1240, 1-19.
- Panning, M. P., Banerdt, W. B., Beghein, C., Carrasco, S., Ceylan, S., Clinton, J. F., . . . Zenhäusern, G. (2023). Locating the largest event observed on Mars with multi-orbit surface waves. *Geophysical Research Letters*, 50(1), e2022GL101270.
- Perrin, C., Jacob, A., Lucas, A., Myhill, R., Hauber, E., Batov, A., . . . Fuji, N. (2022). Geometry and segmentation of Cerberus fossae, Mars: Implications for Marsquake properties. *J. Geophys. Res.: Planets*, 127(1), e2021JE007118. doi: <https://doi.org/10.1029/2021JE007118>
- Phillips, C. B., Burr, D. M., & Beyer, R. A. (2007). Mass movement within a slope streak on Mars. *Geophysical Research Letters*, 34(21). Retrieved from <https://agupubs.onlinelibrary.wiley.com/doi/abs/10.1029/2007GL031577> doi: <https://doi.org/10.1029/2007GL031577>
- Posiolova, L. V., Lognonné, P., Banerdt, W. B., Clinton, J., Collins, G. S., Kawamura, T., . . . Zenhäusern, G. (2022). Largest recent impact craters on Mars: Orbital imaging and surface seismic co-investigation. *Science*, 378(6618), 412-417.
- Roberts, G. P., Matthews, B., Bristow, C., Guerrieri, L., & Vetterlein, J. (2012, February). Possible evidence of paleomarsquakes from fallen boulder populations, Cerberus Fossae, Mars. *J. Geophys. Res. Planets*, 117(E2), n/a-n/a. doi: 10.1029/2011JE003816
- Rosser, N., Kinsey, M., Oven, K., Densmore, A., Robinson, T., Pujara, D. S., . . . Dhital, M. R. (2021). Changing significance of landslide hazard and risk after the 2015 Mw 7.8 Gorkha, Nepal earthquake. *Progress in Disaster Science*, 10, 100159.
- Schorghofer, N., Aharonson, O., Gerstell, M., & Tatsumi, L. (2007). Three decades of slope

- 596 streak activity on mars. *Icarus*, 191(1), 132-140. Retrieved from <https://www>  
 597 [.sciencedirect.com/science/article/pii/S0019103507001960](https://www.sciencedirect.com/science/article/pii/S0019103507001960)  
 598 doi: <https://doi.org/10.1016/j.icarus.2007.04.026>
- 599 Schorghofer, N., Aharonson, O., & Khatiwala, S. (2002). Slope streaks on Mars: Cor-  
 600 relations with surface properties and the potential role of water: Slope streaks on  
 601 Mars. *Geophysical Research Letters*, 29(23), 41–1–41–4. Retrieved 2022-07-14,  
 602 from <http://doi.wiley.com/10.1029/2002GL015889> doi: 10.1029/  
 603 2002GL015889
- 604 Schorghofer, N., & King, C. M. (2011). Sporadic formation of slope streaks on Mars.  
 605 *Icarus*, 216(1), 159–168. Retrieved 2022-07-14, from <https://linkinghub>  
 606 [.elsevier.com/retrieve/pii/S0019103511003459](https://linkinghub.elsevier.com/retrieve/pii/S0019103511003459) doi: 10.1016/  
 607 j.icarus.2011.08.028
- 608 Smith, D. E., Zuber, M. T., Frey, H. V., Garvin, J. B., Head, J. W., Muhleman, D. O., ...  
 609 Sun, X. (2001). Mars orbiter laser altimeter: Experiment summary after the first  
 610 year of global mapping of mars. *Journal of Geophysical Research: Planets*, 106(E10),  
 611 23689-23722.
- 612 Stähler, S. C., Mittelholz, A., Perrin, C., Kawamura, T., Kim, D., Knapmeyer, M., ...  
 613 Banerdt, W. B. (2022). Tectonics of Cerberus Fossae unveiled by marsquakes. *Na-*  
 614 *ture Astronomy*, 6(12), 1376–1386. doi: 10.1038/s41550-022-01803-y
- 615 Sullivan, R., Thomas, P., Veverka, J., Malin, M., & Edgett, K. S. (2001). Mass movement  
 616 slope streaks imaged by the mars orbiter camera. *Journal of Geophysical Research:*  
 617 *Planets*, 106(E10), 23607-23633. doi: <https://doi.org/10.1029/2000JE001296>
- 618 Tanaka, K., Skinner, J., Jr., D., J.M., I., Irwin R.P., Kolb, E., Fortezzo, C., ... Hare, T.  
 619 (2014). Geologic map of mars. *U.S. Geological Survey Scientific, pamphlet 43 p.*  
 620 doi: 10.3133/sim3292
- 621 Tatard, L. (2010). *Statistical analysis of triggered landslides : implications for earthquake*  
 622 *and weather controls* (Unpublished doctoral dissertation). University of Canterbury  
 623 and Université de Grenoble.
- 624 Valantinas, A., Becerra, P., Pommerol, A., Tornabene, L., Affolter, L., Cremonese, G.,  
 625 ... Thomas, N. (2021). CaSSIS color and multi-angular observations of Mar-  
 626 tian slope streaks. *Planetary and Space Science*, 209, 105373. Retrieved 2022-  
 627 07-14, from [https://linkinghub.elsevier.com/retrieve/pii/](https://linkinghub.elsevier.com/retrieve/pii/S0032063321002129)  
 628 [S0032063321002129](https://linkinghub.elsevier.com/retrieve/pii/S0032063321002129) doi: 10.1016/j.pss.2021.105373
- 629 Watters, T. R. (1993). Compressional tectonism on Mars. *Journal of Geophysical Re-*  
 630 *search*, 98(E9), 17049. Retrieved from [http://doi.wiley.com/10.1029/](http://doi.wiley.com/10.1029/93JE01138)  
 631 [93JE01138](http://doi.wiley.com/10.1029/93JE01138) doi: 10.1029/93JE01138
- 632 Wieczorek, M. A., Broquet, A., McLennan, S. M., Rivoldini, A., Golombek, M., Antonan-  
 633 geli, D., ... Banerdt, W. B. (2022). Insight constraints on the global character of the  
 634 martian crust. *Journal of Geophysical Research: Planets*, 127(5), e2022JE007298.

# Supporting Information for "Discussion of possible seismically triggered avalanches after the S1222a Marsquake and S1000a impact event"

Lucas A.<sup>1</sup>, Daubar I. J.<sup>2</sup>, Le Teuff M.<sup>1</sup>, Perrin C.<sup>3</sup>, Kawamura T.<sup>1</sup>, Posiolova L.<sup>4</sup>, Lognonné P.<sup>1</sup>,  
Rodriguez S.<sup>1</sup>, Giardini D.<sup>5</sup>, Sainton G.<sup>1</sup>, Mangeney A.<sup>1</sup>, McEwen A.<sup>6</sup>

## Contents of this file

1. Text S1 to S4
2. Figures S1 to S8

## Text S1. Note on post-marsquake image request and mapping

Once the S1222a event were recorded and a estimate of the location was provided, we investigate the orbital image archive for checking if either this location were falling into a region showing specific surface features (tectonics or avalanche signatures). It appears that this fairly flat region showing a few impact craters, into which, dust avalanches were detectable (Fig. S1). We therefore initiate the mapping using CTX and HiRISE images in order to established the list of location of interest. Then we request to MRO's team to target those specific places. As we focus on maximising the temporal coverage, we utilized all released images from MOC, THEMIS-Vis, CTX and HiRISE sensors. This leads to various conditions of observation (i.e., emission angle, local time etc.) and hence large parallax effects, especially on steep slopes areas where avalanches occur (i.e., typically from 30 to 8 degrees).

Consequently, the accuracy of the ortho-rectification performed with ISIS using either MOLA (Smith et al.; 2001), and/or HRSC DTMs (Neukum and Jaumann; 2004), is not sufficient for accurate sub-pixel co-registration between all the images, even with bundle adjustment. This is an important aspect because as a result no automatic method could be used successfully (i.e., all of our principal component analysis (PCA) and Convolutional Neural Network (CNN) attempts failed to reach the required accuracy that could be achieved with human inspection).

We manually map all avalanches in the region shown in Fig. 1 in a Geographical Information System (GIS). Then each pair of overlapping images (mostly CTX/CTX pairs, but we also considered CTX/HiRISE and HiRISE/HiRISE overlapping observations) leads to a detection of new (or absence of new) avalanches. This mapping work has been conducted by two independent people to compare and validate the results. Although non-MRO images offer a greater historical depth (~15 Earth years), the resolutions are very different between these sensors. Hence, over the 2008-2022 period, only CTX and HiRISE are considered. We down-sample the HiRISE data to 6 m/pixel, a pixel scale close to CTX's.

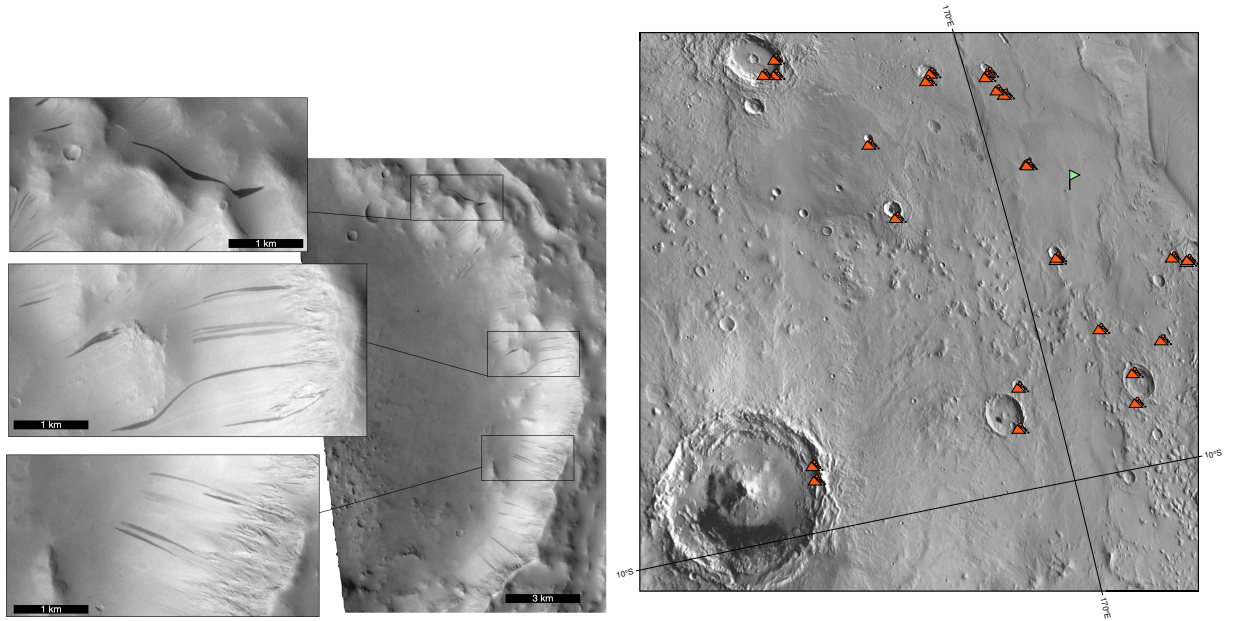


Figure S1: Location of the pre-event avalanche mapping once an estimate of the S1222a location was provided. (left panel) close up on CTX G10\_021978\_1748\_XI\_05S192W (2011-04-05).

As well known, the brightness of these streaks is usually inversely proportional to their age. The darker they are, the more recently they formed (Sullivan et al.; 2001). Note that we observe a very slow fading rate in this area, as some image pairs spanning 18 Earth years still show the same avalanches. Such a low fading rate allows us to estimate the long-term avalanche formation rate without concern that ongoing fading would significantly affect our measured rates (Aharonson et al.; 2003). Additionally, this slow fading rate is in good agreement with the dust activity reported in this region (Battalio and Wang; 2021).

For the sake of comparison, the fading rate of dust devil tracks at the InSight landing site was also measured. There, dust devil tracks fade in a few months to almost two terrestrial years (Perrin et al.; 2020). Notwithstanding, these are not formed by the same processes and thus might not fade at the same rates, in particular since avalanches remove a thicker layer of dust cover compared to dust devils. Other types of albedo features fade at different rates on Mars. For example, blast zones around new impacts have a median fading lifetime of 8 Mars years (Daubar et al.; 2016), while dust devil tracks and rover tracks fade much more quickly as they remove dust more superficially (Balme et al.; 2003; Verba et al.; 2010; Geissler et al.; 2010). To compare the same type of feature as studied here, other slope streaks have shown gradual fading over approximately 20 Mars years (e.g., Schorghofer et al.; 2007; Bergonio et al.; 2013).



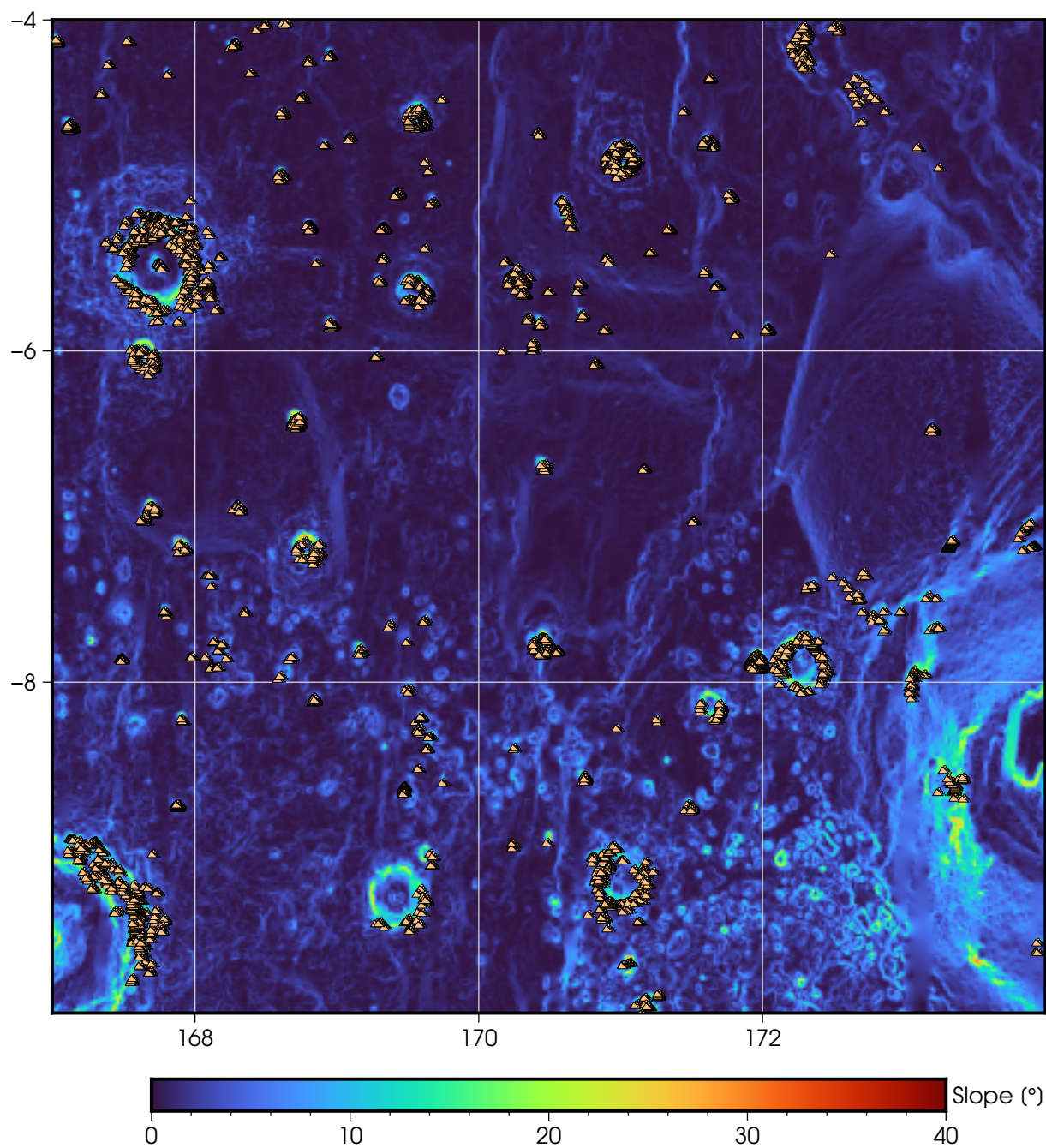


Figure S2: Slope map derived from MOLA 128ppd (Smith et al.; 2001). Orange symbols show location of avalanches over the 2005-2021 period.

## Text S2. Note on the thermal inertia

The thermal inertia ( $\Gamma$ ) is a complex data set that is not directly obtained from observations (see <https://astrogeology.usgs.gov/maps/mars-themis-derived-global-thermal-inertia-mosaic>). Numerous factors contribute to thermal inertia. In our study, however, the emphasis is on the consistency of observations. We have conducted thorough verifications to ensure homogeneity in the slopes within the areas where avalanches were mapped. This implies that any topographic effects would uniformly impact these areas. By using flat terrain as a reference for comparison, the validity of our comparative analysis of the  $\Gamma^* = \Gamma_{avalanche} / \Gamma_{plain}$  across the avalanche-affected areas is maintained. The map of the  $\Gamma$  is given in Figure S3.

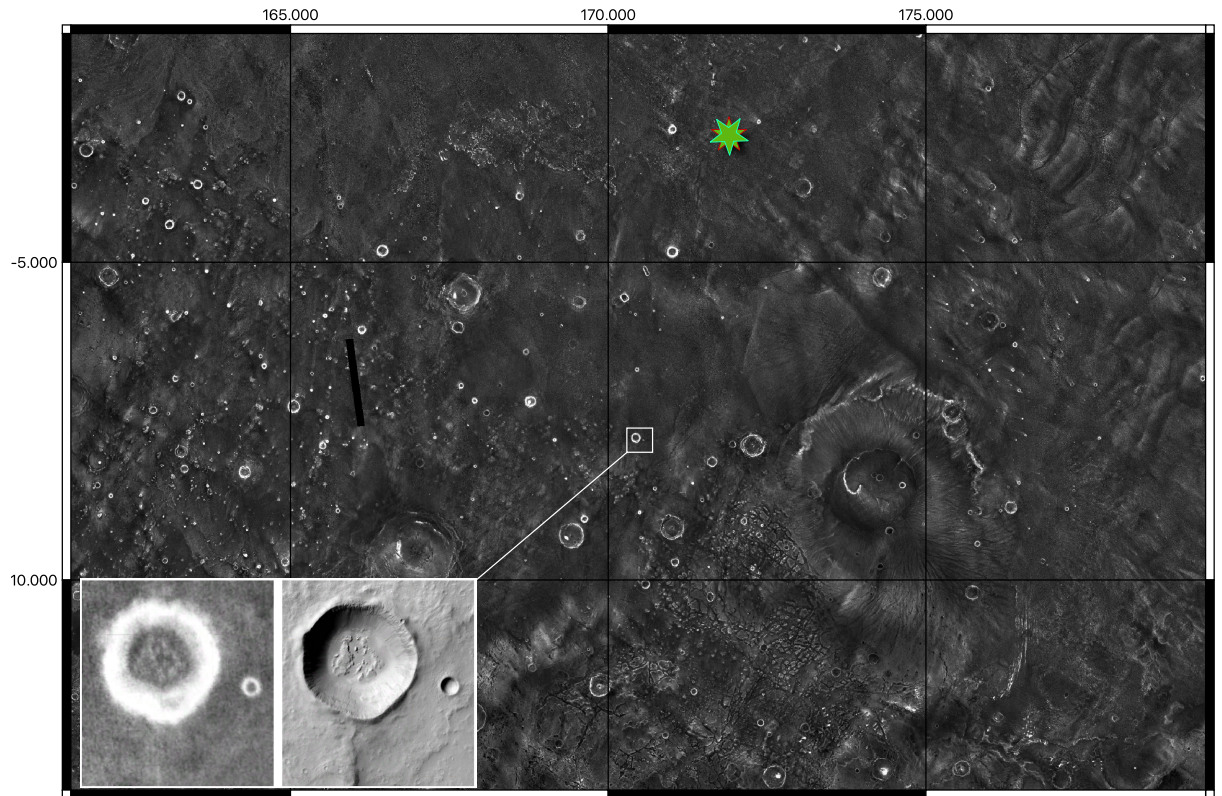


Figure S3: Apparent thermal inertial map derived from THEMIS-IR over the region of interest provided by the USGS. Green star is the epicentral location estimated from Kawamura et al. (2023). Inset shows a close-up on a crater presenting dust avalanches with thermal inertia and its visible counterpart from CTX.

### Text S3. Note on triggering factors

Avalanche motion treated as a single-phase dry granular flow with Coulomb-type behaviour can be described by a two-dimensional Saint-Venant system. Hence, the transition between a static state and a flowing state is modelled by introducing a threshold allowing the material to flow. The friction forces  $f(x, y, t)$  must satisfy

$$||f(x, y, t)|| \leq \mu \rho g h, \quad (1)$$

where  $\mu$  is the friction coefficient,  $\rho$  the density,  $g$  acceleration due to the gravity, and  $h$  the thickness. This has been shown to quantitatively capture debris and rock avalanche morphodynamics on Mars (Lucas; 2010; Lucas and Mangeney; 2007; Lucas et al.; 2011, 2014). Hence, this transition is sensitive to ground acceleration or dust deposition. To evaluate the stability of a slope composed of Martian dust, taking into account the potential cohesion of dust due to electrostatic forces, one can use the Coulomb failure criterion

$$\tau = c + \sigma_n \tan(\phi), \quad (2)$$

where:  $\tau$  is the shear stress,  $c$  is the cohesion of the material,  $\sigma$  is the normal stress, and  $\phi$  is the angle of internal friction (where  $\mu = \tan(\phi)$ ). The normal stress on a slope is calculated as:

$$\sigma_n = \rho g h \cos^2(\theta), \quad (3)$$

where  $\rho$  is the density of the material,  $g$  is the acceleration due to the gravity,  $h$  is the depth of the material, and  $\theta$  is the slope angle.

#### • Triggering by dust deposition

The additional shear stress  $\delta\tau$  due to an additional height  $\delta h$  of deposition is estimated by:

$$\delta\tau = \rho g \delta h \sin(\theta) \cos(\theta) \quad (4)$$

By rearranging the aforementioned equations, the additional deposit height necessary for slope failure, denoted as  $\delta h$ , can be calculated. One can perform a parametric exploration accounting for the following parameter ranges estimated from soil mechanics experiments recently performed with HP<sup>3</sup> on InSight Spohn et al. (2022a,b): initial dust thickness  $h = \{10 \text{ cm}, 2\text{m}\}$ , slope angle  $\theta = 30^\circ$ , friction angle  $\phi = \{12^\circ, 25^\circ, 35^\circ\}$  and cohesion  $c = \{0, 12\}$  (kPa). The additional dust height  $\delta h$  required to trigger failure ranges from millimetric to metric scales as illustrated in the Fig. S4. These ranges can be compared to the typical dust deposition rates observed on the ground from both rovers and landers. As a matter of fact, dust deposition of a few particles radius per 100 sols are observed at the MER rover locations (Kinch et al.; 2007). By considering the 140 sols between the closest image pair ( $L_s = \{80; 220\}$ ) and the typical grain size radii discussed by Kinch et al. (2007), would lead to  $140 \text{ sols} \times 3 \text{ radii}/100 \text{ sols} \times 1.5 \mu\text{m} = 6.30 \mu\text{m}$ , which is 3 folds smaller than the lower bound discussed previously. Accounting for larger particle radii ( $r=60 \mu\text{m}$ ) as it was assessed around the InSight landing site (Chen-Chen et al.; 2023), the dust accumulation would be around  $250 \mu\text{m}$  over the 140 sols period, which is comparable to the dust settling rate which was recorded to be  $1 \mu\text{m}/\text{sols}$  at Phoenix landing site (Drube et al.; 2010). Still, such extreme values of dust rate would be insufficient.

The dust rate at the S1222a location can be estimated from GCMs results, by dividing the total dust deposit over the 140 sols period by the density of the material. Considering a of  $1600 \text{ kg.m}^{-3}$  and a typical mean dust deposition of  $0.5 \times 10^{-9} \text{ kg.m}^{-2}.\text{s}^{-1}$  (Figure S5), the deposit accumulated is of about  $7 \mu\text{m}$ , which in agreement to MER's location observations as shown in Kinch et al. (2007). Additionally, pre-event images display wind streaks oriented northward, associated with small impact craters. However, post-event images do not show any changes, casting doubt on the wind's ability to transport dust within the observed time span (Fig S6). Predictions from GCM indicate surface wind speed below  $3 \text{ m.s}^{-1}$  if we except slope winds over Apollinaris Mons (Figure S7). Finally, the orientation of the slopes on which avalanches are observed, whether in images before or after event S1222a, show the same distribution as that of steep slopes ( $>10^\circ$ ), which allows us to rule out, once again, any connection with the action of the wind (Fig. S8).

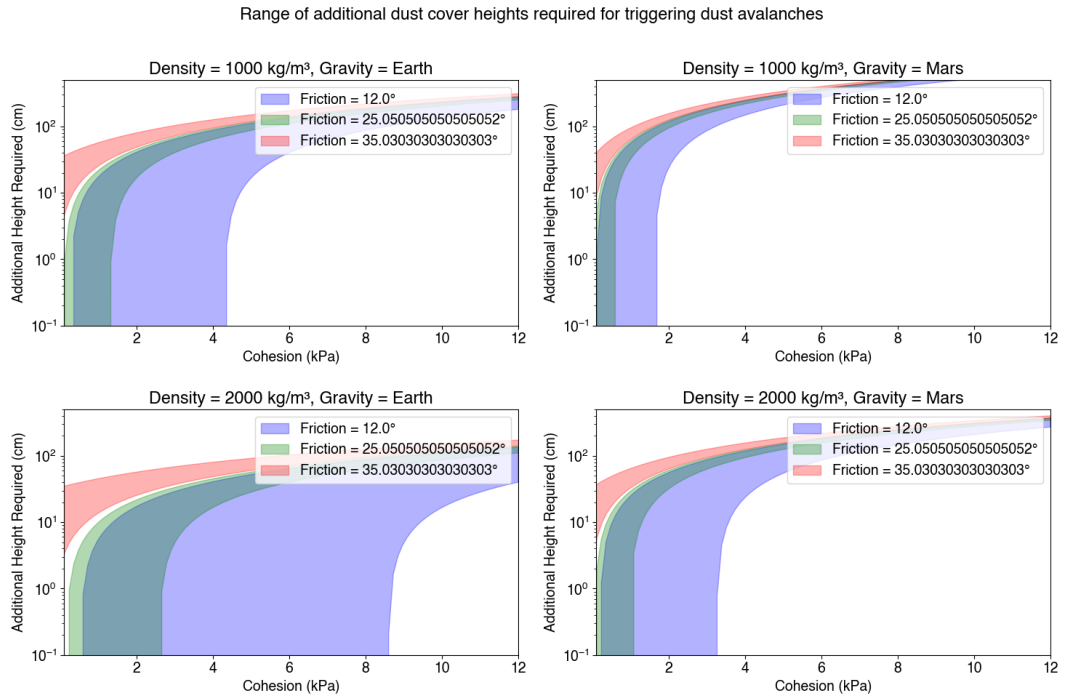


Figure S4: Estimation of the required additional dust heights for reaching slope failure under various conditions. The bounds for each computation are corresponding to an initial dust thickness ranging from 10 cm (lower bounds) up to 2 meters (upper bounds) and a slope angle of  $30^\circ$ .



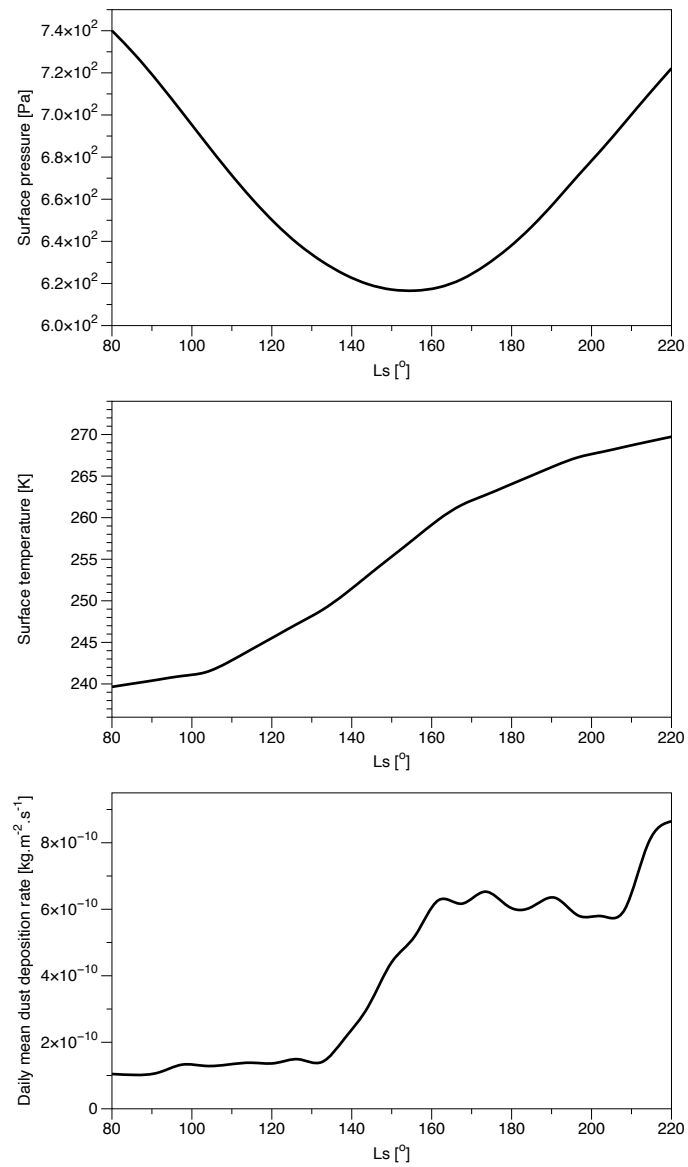


Figure S5: LMD GCM predictions for (top) Surface atmospheric pressure at the S1222a area computed at 2pm, from Ls ranging from 80 to 220; (center) Surface temperature; (bottom) Daily mean dust deposition rate for the same period. Plots generated from the Mars Climate Database (c) LMD/LATMOS/OU/IAA/ESA/CNES.

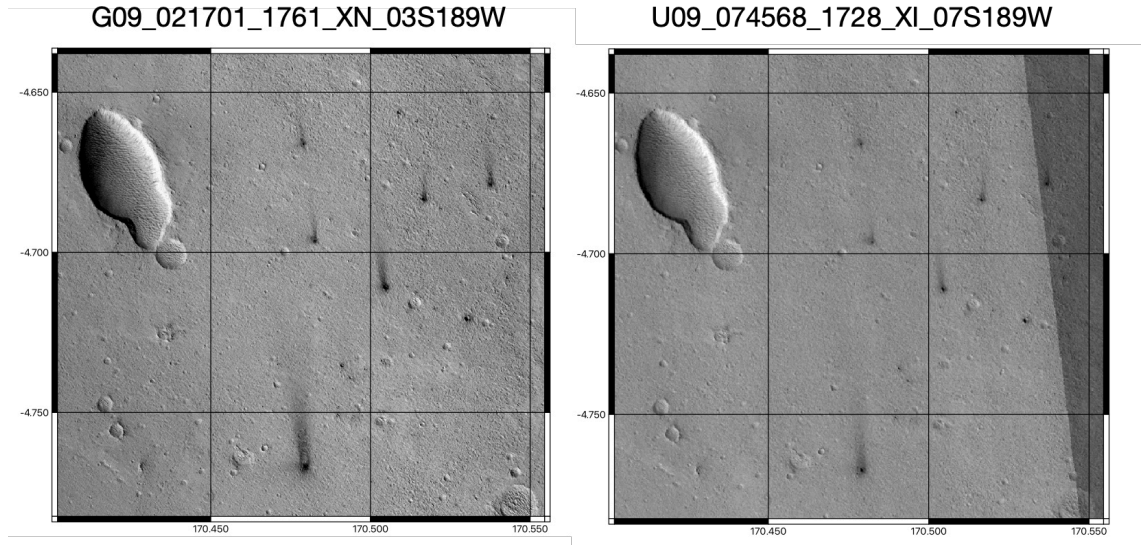


Figure S6: Wind streaks as observed from both pre- and post- S1222a event images.

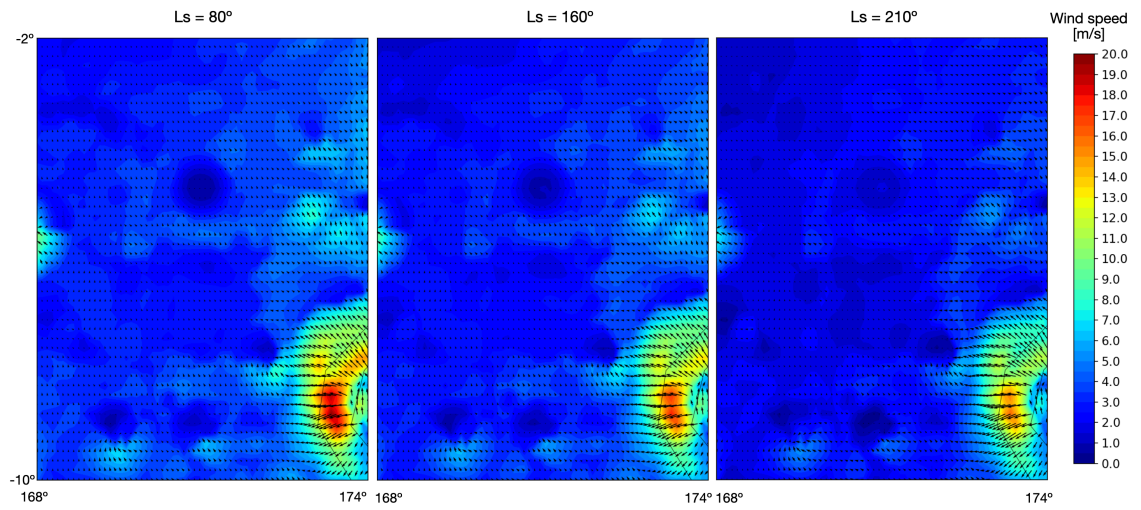


Figure S7: Surface wind speed predicted from GCM at different Ls. Plots generated from the Mars Climate Database (c) LMD/LATMOS/OU/IAA/ESA/CNES.



Figure S8: Distribution of steep slopes orientation ( $>10^\circ$ ) from MOLA data at 128ppd over the region of the S1222a event, covered by figure S2 (in blue). Orientation at avalanche locations from pre-event images (orange) and post-event images (red).

### • Triggering by atmospheric pressure variation

In order to evaluate the atmospheric pressure variation required to initiate slope failure, we need to focus on the change in shear stress. The pressure variation, in this context, is essentially the increase in shear stress needed to reach the failure point. To find the pressure variation required for failure, one needs to calculate the difference between the current shear stress due to the weight of the material and the shear strength (given by the Coulomb failure criterion). This difference represents the additional shear stress required to reach the failure condition. For the specified parameters (cohesion of 1000 Pa, friction angle of 30 degrees, density of 1600 kg/m<sup>3</sup>, height of 1 meter, slope angle of 30 degrees, and Martian gravity), the calculated pressure variation (additional shear stress) required to initiate slope failure is approximately 1000 Pascals. In comparison, the typical pressure variations due to turbulence observed at the InSight landing site are of about a few 10's of Pa, which is two folds smaller than the required pressure variations.

### • Triggering by ground acceleration

To evaluate how ground acceleration from seismic activity, could contribute to reaching the slope failure condition, we need to consider the additional shear stress induced by this acceleration. One can approach this by considering the pseudostatic analysis, where the seismic force is simplified as a static force acting on the slope. The additional shear stress ( $\delta\tau$ ) due to ground acceleration ( $a$ ) can be estimated using the formula:

$$\delta\tau = \rho a h \sin(\theta), \quad (5)$$

where  $a$  is the horizontal ground acceleration. The total shear stress acting on a slope is the cumulative effect of the inherent shear stress, which is a consequence of gravitational forces, and the additional shear stress induced by ground acceleration. A slope is prone to failure when this combined shear stress surpasses the material's shear strength, as defined by the Coulomb failure criterion. Continuing with the same parameters as before — cohesion ( $c$ ) at 1000 Pa, internal friction angle at 30 degrees, density at 1600 kg.m<sup>-3</sup>, and a slope angle of 30 degrees — we consider a hypothetical ground acceleration of 0.5 m.s<sup>-2</sup>, which is 15% of Martian gravity (A typical  $M_w$  5 on Earth leads to 10% of terrestrial gravity, (e.g., Sandron et al.; 2019)). Under these conditions, an initial material thickness of 3 meters results in the total shear stress beginning to surpass the shear strength. This indicates a condition likely to lead to slope failure.

A key factor influencing the outcome in terms of both total shear stress and shear strength is the initial height of the material on the slope. Within our model's framework, the gravitational shear stress and the extra shear stress from ground acceleration are both directly proportional to the material's height. Consequently, an increase in height leads to a corresponding rise in both types of stress. However, the rates at which they increase may vary. This variance plays a crucial role in determining how changes in height influence the probability of slope failure. This aspect can be related to the fact the thermal properties, as shown in the main text, seems to control the increase of the avalanche rate.

The ground acceleration associated with an earthquake is generally evaluated through the PGA (Peak Ground Acceleration), the maximum amplitude recorded during an earthquake. On the zeroth-order, this value will depend on the epicentral distance. Following Gomberg et al. (2006); Gomberg and Felzer (2008), we can relate the ground motion  $G$  with epicentral distance  $\Delta$  through this simple relation:

$$PGA(\Delta) = \frac{K}{(\alpha + \Delta)^2}, \quad (6)$$

where  $K$  and  $\alpha$  are empirical parameters (Gomberg and Felzer; 2008). Nonetheless, as on Earth, avalanches or rockfalls occur in response to a combination and cumulative forcings acting at different time scales including gravity, weathering and chemical effects, thermal, meteorological, seismic or volcanic activities (e.g., Tatard; 2010).

#### Text S4. Note on the inversion method and uncertainties

Following Mosegaard and Tarantola (1995), we can use inverse problem method to estimate what is the epicentral location that best explain the avalanche rate derived from orbital imagery.

As the "direct problem" consisting in predicting the d-values that we should observe when we make observations on a given system, such system can be described by a vector  $\mathbf{m}$  of parameters, such as  $\mathbf{m} = \{m_1, m_2, \dots, m_i\}$ . We can define a probability density  $\sigma(\mathbf{m})$  that combines the a priori  $\rho(\mathbf{m})$  information with the information provided by the experimental measurements (the data vector) and the information provided by the physics of the problem (i.e., the model). Hence,  $\sigma(\mathbf{m})$  is called the posterior information. It is the combination of all the information we have and reads:

$$\sigma(\mathbf{m}) = k\rho(\mathbf{m})L(\mathbf{m}), \quad (7)$$

with  $k$  being a normalization constant (=1) and  $L(\mathbf{m})$  the likelihood function accounting for a Laplacian experimental uncertainties, which reads:

$$L(\mathbf{m}) = \exp \left[ - \sum_i \frac{\|G^i(\mathbf{m}) - d_{obs}^i\|}{\sigma_i} \right], \quad (8)$$

where  $G^i(\mathbf{m})$  is the prediction by the model  $G(\mathbf{m})$  of the  $i^{th}$  observation,  $d_{obs}^i$  is the  $i^{th}$  observation with its associated uncertainties  $\sigma_i$ . In this study, the model  $G(\mathbf{m})$  is provided after Livio and Ferrario (2020) which relates the avalanche (or landslides in their paper) distribution with the epicentral distance  $\Delta$ :

$$G(\mathbf{m}) = N_{ava} = a \exp \left[ - \left( \frac{\Delta - b}{c} \right)^2 \right], \quad (9)$$

where  $N_{ava}$  is the avalanches number triggered by the seismic event, where  $\mathbf{m} = \{a, b, c\}$ , with  $a$  the peak amplitude of the distribution,  $b$  the distribution peak distance to the epicenter, and  $c$  the distribution width.

Hence, we randomly explore the longitude-latitude space ( $\text{Lon} \in [166, 175]$  and  $\text{Lat} \in [-10, -1]$ ) over 1 million runs. For each run, compute the epicentral distance for each avalanche's area that meet both conditions ( $\Delta t; 1.5 \text{ MYear}$  and  $\Gamma^* < 450$ ). Then, we fit the equation 9 on the observed  $N_{ava}$  vs  $\Delta$  (expressed in euclidean distances and accounting for Mars flattening) using a non-linear least squares method. Finally, we compute the maximum likelihood function from equation 8 which accounts for a Laplacian distribution of uncertainties on the avalanche number.

The uncertainties on the avalanche rate  $q$  is computed after Aharonson et al. (2003), which reads:

$$\sigma = \left\langle \langle q - \langle q \rangle \rangle^{1/2} \right\rangle^2 = \frac{\langle q \rangle}{\sqrt{1 + \sum_i \Delta n_i}}, \quad (10)$$

with  $\langle q \rangle$  being the expectation value of  $q$ , which reads:

$$\langle q \rangle = \frac{1 + \sum \Delta n_i}{\sum_i n_i \Delta t_i}. \quad (11)$$

## References

- Aharonson, O., Schorghofer, N. and Gerstell, M. F. (2003). Slope streak formation and dust deposition rates on Mars: Martian slope streak formation rates, *Journal of Geophysical Research: Planets* **108**(E12).
- Balme, M. R., Whelley, P. L. and Greeley, R. (2003). Mars: Dust devil track survey in argyre planitia and hellas basin, *Journal of Geophysical Research: Planets* **108**(E8).
- Battalio, M. and Wang, H. (2021). The Mars Dust Activity Database (MDAD): A comprehensive statistical study of dust storm sequences, *Icarus* **354**: 114059.
- Bergonio, J. R., Rottas, K. M. and Schorghofer, N. (2013). Properties of martian slope streak populations, *Icarus* **225**(1): 194–199.
- Chen-Chen, H., Pérez-Hoyos, S., Sánchez-Lavega, A. and Peralta, J. (2023). Characterisation of deposited dust particles on mars insight lander instrument context camera (icc) lens, *Icarus* **392**: 115393.
- Daubar, I., Dundas, C., Byrne, S., Geissler, P., Bart, G., McEwen, A., Russell, P., Chojnacki, M. and Golombek, M. (2016). Changes in blast zone albedo patterns around new martian impact craters, *Icarus* **267**: 86–105.
- Drube, L., Leer, K., Goetz, W., Gunnlaugsson, H. P., Haspang, M. P., Lauritsen, N., Madsen, M. B., Sørensen, L. K. D., Ellehoj, M. D., Lemmon, M. T., Morris, R. V., Blaney, D., Reynolds, R. O. and Smith, P. H. (2010). Magnetic and optical properties of airborne dust and settling rates of dust at the phoenix landing site, *Journal of Geophysical Research: Planets* **115**(E5).
- Geissler, P. E., Sullivan, R., Golombek, M., Johnson, J. R., Herkenhoff, K., Bridges, N., Vaughan, A., Maki, J., Parker, T. and Bell, J. (2010). Gone with the wind: Eolian erasure of the mars rover tracks, *Journal of Geophysical Research: Planets* **115**(E7).
- Gomberg, J. and Felzer, K. (2008). A model of earthquake triggering probabilities and application to dynamic deformations constrained by ground motion observations, *Journal of Geophysical Research: Solid Earth* **113**(B10).
- Gomberg, J., Felzer, K. R. and Brodsky, E. E. (2006). Earthquake dynamic triggering and ground motion scaling.
- Kawamura, T., Clinton, J., Zenhäusern, G., Ceylan, S., Horleston, A., Dahmen, N., Duran, C., Kim, D., Plasman, M., Stähler, S., Euchner, F., Charalambous, C., Giardini, D., Davis, P., Sainton, G., Lognonné, P., Panning, M. and Banerdt, W. (2023). S1222a - the largest Marsquake detected by InSight, *Geophysical Research Letters*.

- Kinch, K. M., Sohl-Dickstein, J., Bell III, J. F., Johnson, J. R., Goetz, W. and Landis, G. A. (2007). Dust deposition on the mars exploration rover panoramic camera (pancam) calibration targets, *Journal of Geophysical Research: Planets* **112**(E6).
- Livio, F. and Ferrario, M. F. (2020). Assessment of attenuation regressions for earthquake-triggered landslides in the italian apennines: insights from recent and historical events, *Landslides* **17**(12): 2825–2836.
- Lucas, A. (2010). *Dynamique des instabilités gravitaires par modélisation et télédétection: Applications aux exemples martiens*, Theses, Institut de physique du globe de paris - IPGP.  
**URL:** <https://tel.archives-ouvertes.fr/tel-00503212>
- Lucas, A. and Mangeney, A. (2007). Mobility and topographic effects for large valles marineris landslides on mars, *Geophysical Research Letters* **34**(10).
- Lucas, A., Mangeney, A. and Ampuero, J. P. (2014). Frictional velocity-weakening in landslides on earth and on other planetary bodies, *Nature Communications* **5**(1): 3417.
- Lucas, A., Mangeney, A., Mège, D. and Bouchut, F. (2011). Influence of the scar geometry on landslide dynamics and deposits: Application to martian landslides, *Journal of Geophysical Research: Planets* **116**(E10).
- Mosegaard, K. and Tarantola, A. (1995). Monte carlo sampling of solutions to inverse problems, *Journal of Geophysical Research: Solid Earth* **100**(B7): 12431–12447.
- Neukum, G. and Jaumann, R. (2004). The high resolution stereo camera of mars express, *ESA Special Publication* **1240**: 1–19.
- Perrin, C., Rodriguez, S., Jacob, A., Lucas, A., Spiga, A., Murdoch, N., Lorenz, R., Daubar, I. J., Pan, L., Kawamura, T., Lognonné, P., Banfield, D., Banks, M. E., Garcia, R. F., Newman, C. E., Ohja, L., Widmer-Schmid, R., McEwen, A. S. and Banerdt, W. B. (2020). Monitoring of dust devil tracks around the insight landing site, mars, and comparison with in situ atmospheric data, *Geophysical Research Letters* **47**(10): e2020GL087234.
- Sandron, D., Santulin, M., Tamaro, A., Orci, C., Benedetti, G., Castellaro, S., Romeo, R., Rebez, A., Grimaz, S., Malisan, P., Guadagnini, G., Sciascia, F. and Slejko, D. (2019). Seismic parameter design assessment for the kribi deep seaport in cameroon, *Bulletin of Earthquake Engineering* **17**.
- Schorghofer, N., Aharonson, O., Gerstell, M. and Tatsumi, L. (2007). Three decades of slope streak activity on mars, *Icarus* **191**(1): 132–140.
- Smith, D. E., Zuber, M. T., Frey, H. V., Garvin, J. B., Head, J. W., Muhleman, D. O., Pettengill, G. H., Phillips, R. J., Solomon, S. C., Zwally, H. J., Banerdt, W. B., Duxbury, T. C., Golombek, M. P., Lemoine, F. G., Neumann, G. A., Rowlands, D. D., Aharonson, O., Ford, P. G., Ivanov, A. B., Johnson, C. L., McGovern, P. J., Abshire, J. B., Afzal, R. S. and Sun, X. (2001). Mars orbiter laser altimeter: Experiment summary after the first year of global mapping of mars, *Journal of Geophysical Research: Planets* **106**(E10): 23689–23722.

- Spohn, T., Hudson, T. L., Marteau, E., Golombek, M., Grott, M., Wippermann, T., Ali, K. S., Schmelzbach, C., Kedar, S., Hurst, K., Trebi-Ollennu, A., Ansan, V., Garvin, J., Knollenberg, J., Müller, N., Piqueux, S., Lichtenheldt, R., Krause, C., Fantinati, C., Brinkman, N., Sollberger, D., Delage, P., Vrettos, C., Reershemius, S., Wisniewski, L., Grygorczuk, J., Robertsson, J., Edme, P., Andersson, F., Krömer, O., Lognonné, P., Giardini, D., Smrekar, S. E. and Banerdt, W. B. (2022b). The insight HP<sup>3</sup> penetrator (mole) on mars: Soil properties derived from the penetration attempts and related activities, *Space Science Reviews* **218**(8): 72.
- Spohn, T., Hudson, T., Witte, L., Wippermann, T., Wisniewski, L., Kedziora, B., Vrettos, C., Lorenz, R., Golombek, M., Lichtenheldt, R., Grott, M., Knollenberg, J., Krause, C., Fantinati, C., Nagihara, S. and Grygorczuk, J. (2022a). The InSight-HP<sup>3</sup> mole on Mars: Lessons learned from attempts to penetrate to depth in the martian soil, *Advances in Space Research* **69**.
- Sullivan, R., Thomas, P., Veverka, J., Malin, M. and Edgett, K. S. (2001). Mass movement slope streaks imaged by the mars orbiter camera, *Journal of Geophysical Research: Planets* **106**(E10): 23607–23633.
- Tatard, L. (2010). *Statistical analysis of triggered landslides : implications for earthquake and weather controls*, PhD thesis, University of Canterbury and Université de Grenoble.
- Verba, C. A., Geissler, P. E., Titus, T. N. and Waller, D. (2010). Observations from the high resolution imaging science experiment (hirise): Martian dust devils in gusev and russell craters, *Journal of Geophysical Research: Planets* **115**(E9).